

## TABLE OF CONTENTS

<b>I</b>	<b>Introduction and Motivation</b>	<b>5</b>
<b>1</b>	<b>Introduction . . . . .</b>	<b>6</b>
1.1	Description of solid breeder blankets . . . . .	7
1.1.1	Tritium breeding . . . . .	8
1.1.2	Solid breeder design . . . . .	10
1.1.3	Material candidates and related phenomena . . . . .	11
1.2	Importance of pebble bed integrity and motivation . . . . .	12
1.3	Scope of the work . . . . .	12
<b>II</b>	<b>Literature Review</b>	<b>16</b>
<b>2</b>	<b>Pebble Interaction Analysis: Theory . . . . .</b>	<b>17</b>
2.1	Hertz theory for normal contact of spheres . . . . .	17
<b>3</b>	<b>Pressure drop across packed beds . . . . .</b>	<b>23</b>
<b>4</b>	<b>Heat transfer in packed beds . . . . .</b>	<b>24</b>
4.1	Inter-particle heat conduction . . . . .	26
4.2	Nusselt number for spheres in packed beds . . . . .	28
4.2.1	Packed bed correlations: Nellis and Klein . . . . .	29
4.2.2	Packed beds correlation: Whitaker . . . . .	30
4.2.3	Single pebble correlations . . . . .	31
4.3	Jeffreson correction to lumped capacitance method . . . . .	31

4.3.1	Lumped capacitance solution for sphere . . . . .	32
4.3.2	Exact solution for sphere . . . . .	35
4.3.3	Jeffreson correction for sphere . . . . .	39
4.4	Radiative transfer with neighboring particles . . . . .	41
<b>III</b>	<b>Methodology</b>	<b>44</b>
<b>5</b>	<b>Modeling Discrete Element Method (DEM)</b> . . . . .	<b>45</b>
5.1	Background . . . . .	45
5.2	Particle dynamics . . . . .	46
5.2.1	Particle kinematics . . . . .	46
5.2.2	Linear spring-dashpot model . . . . .	47
5.2.3	Hertzian non-linear spring dashpot model . . . . .	49
5.2.4	Time integration . . . . .	50
5.3	Granular heat transfer . . . . .	51
5.3.1	Thermal expansion . . . . .	52
5.4	Stability study . . . . .	52
5.4.1	Critical dynamic timestep . . . . .	53
5.4.2	Critical thermal timestep . . . . .	55
5.4.3	Simulation acceleration with scaled material properties . . . . .	56
5.5	Pebble failure modeling . . . . .	56
5.6	DEM solver . . . . .	57
5.6.1	Numerical Implementation Overview . . . . .	57
5.6.2	other solver info . . . . .	58

<b>6 Modeling coupled computational fluid dynamics and discrete element method (CFD-DEM) . . . . .</b>	<b>60</b>
6.1 Numerical Methodology . . . . .	60
6.1.1 DEM . . . . .	61
6.1.2 Volume-averaged CFD Helium . . . . .	63
6.1.3 Modeling Setup and Procedure . . . . .	64
<b>7 Modeling lattice-Boltzmann Method (LBM) . . . . .</b>	<b>66</b>
<b>IV Cases studied . . . . .</b>	<b>67</b>
<b>8 DEM studies . . . . .</b>	<b>68</b>
8.1 DEM study: effective conductivity with disrupted packing . . . . .	68
8.1.1 Material properties . . . . .	68
8.1.2 Methodology . . . . .	69
8.1.3 Pebble Bed Heat Transfer: Test Case . . . . .	70
8.2 Study of Young's Modulus . . . . .	78
8.2.1 Numerical experiments setup . . . . .	78
8.2.2 Results . . . . .	79
8.2.3 Conclusions . . . . .	82
8.3 Conclusions . . . . .	83
<b>9 CFD-DEM studies . . . . .</b>	<b>85</b>
9.1 Pressure Drop . . . . .	85
9.2 Effective thermal conductivity from CFD-DEM . . . . .	85
9.2.1 Stagnant interstitial fluid . . . . .	85

9.2.2	Purge gas . . . . .	85
<b>10</b>	<b>LBM studies . . . . .</b>	<b>91</b>
<b>11</b>	<b>Pebble Interaction Analysis: Experimental Relationships . . . . .</b>	<b>92</b>
11.1	Elasticity reduction factor . . . . .	92
11.1.1	Elasticity reduction factor . . . . .	93
11.2	Strain energy measurements . . . . .	101
11.3	Linking interactions with strain energy . . . . .	101
11.3.1	Pebble crushing predictions . . . . .	104
<b>V</b>	<b>Future Work</b>	<b>105</b>
<b>VI</b>	<b>Appendices</b>	<b>106</b>
<b>A</b>	<b>Sphere with heat generation . . . . .</b>	<b>107</b>
A.1	Transformations . . . . .	108
A.2	Solution . . . . .	109
A.3	Energy . . . . .	113

**Part I**

# **Introduction and Motivation**

# CHAPTER 1

## Introduction

From the very beginning of fusion reactor studies, researchers recognized the necessity of generating tritium inside the thermonuclear reactor. In the attempt to force the fusion neutron to collide with a lithium atom and thus produce a tritium atom, a design approach was proposed by Abdou et al<sup>7</sup> in 1975 wherein the plasma would be surrounded by a ‘blanket’ of nonmobile, solid lithium. The lithium would be combined with ceramic materials to maintain the solid phase at elevated temperatures and exist in a packed bed (also referred to as pebble bed) form.

To date, lithiated ceramic pebbles have been chosen by many participants in ITER experiments as a material to be used for tritium generation.<sup>?, ?, ?, ?</sup> The advantages of the pebble bed design include ease of assembling the solid into complex geometries, ease of tritium extraction from the porous bed via an interstitial purge of helium, and with the small size of pebbles being more resilient to thermal stresses than a solid brick of lithiated ceramic. Naturally, however, the pebble bed form carries with it many of its own disadvantages that must be understood and overcome.

In thermonuclear fusion reactors, the ceramic pebble beds will be contained and cooled by a structural material (currently it is foreseen to use ferritic or austenitic steel). As nuclear energy is deposited into the poorly conductive ceramic breeder the temperature rises well above the containment structure and subsequently attempts to swell from thermal expansion but is confined due to the structure. This simple action is the root of many design issues for the pebble bed. For one, the confined expansion directly leads to cracking of individual pebbles from the high contact stresses. The packing structure response depends on the extent

and modes of cracking and the thermophysical properties likewise change. Second, thermal ratcheting or thermally-induced bed creep can lead to evolutions in thermophysical properties even in the absence of cracked pebbles. Finally, as the thermophysical properties evolve, global or local bed temperatures change and ultimately the tritium release characteristics of the bed deviate from any prediction one may have had from the initial packing of the ceramic pebble bed.

Alleviating any of the issues that may plague the ceramic breeder all boil down to requiring temperature control via an understanding and of the morphological changes of the ceramic packed beds and their interaction with the interstitial purge gas and structural container. In this work we introduce enhancements and new elements to build upon the understanding from ceramic breeder models of past research efforts.

In this chapter we will introduce more detail on the fundamental features of a fusion reactor blanket design as it relates to a breeder blanket design. Following that will be a list of the research objectives of this study. In Part II (§§ 2 to 4) we survey the state of the art in analysis of ceramic pebble beds, contact mechanics, and modeling thermal and mechanical interactions of packed beds. In Part III (§§ 5 to 7) we outline the numerical methodology of the models and tools used in this study, namely: the discrete element method (DEM), coupled computational fluid dynamics and the discrete element method (CFD-DEM), and an integrated lattice-Boltzmann method (LBM). We employ our physics knowledge and numerical tools to cover a range of studies in Part IV (§§ 8 to 11). Finally, in Part V, we discuss the future of the current work and any limitations or interesting work that was beyond the scope of this dissertation.

## 1.1 Description of solid breeder blankets

Before describing the solid breeder blanket and the design requirements, it is worth reviewing the major features of a fusion reaction and potential reactor. The current, worldwide choice for fusion reaction is deuterium-tritium (D-T). The choice is based on D-T having a high reaction probability at the lowest ion temperature, high energy yield, fuel availability, and

reaction products (how harmless are the daughter products). The D-T cycle is



While Deuterium ( $D$ , or  ${}^2\text{H}$ ), is a stable isotope and is naturally occurring in an average abundance of 0.015 mole percent in water on Earth. Tritium ( $T$ , or  ${}^3\text{H}$ ), conversely, is radioactive with a half life of only about 12.32 years; naturally decaying as  $\beta^-$  emitter (no  $\gamma$  rays),



### 1.1.1 Tritium breeding

Owing to its short half life, any naturally occurring tritium would decay at such a rapid pace it can never accumulate. Because of this, it will need to be generated artificially (bred) if it is to be used as a fuel in a fusion reactor. Fusion reactor designs receiving the most attention from the international community include a tritium breeding blanket as an integral component for maintaining self-sufficiency of the reaction. It is achieved with lithium. When natural lithium interacts with a neutron, its two most common isotopes have the following reaction



where we have used the common short-hand of  $\alpha$  in place of the helium nucleus. The cross-sections of the lithium reactions are given in Fig. 1.1

Serendipitously, the D-T reaction itself produces a high energy neutron (see Eq. 1.1). If we assume that  $D$  is essentially limitless (on the scale of human consumption) and have

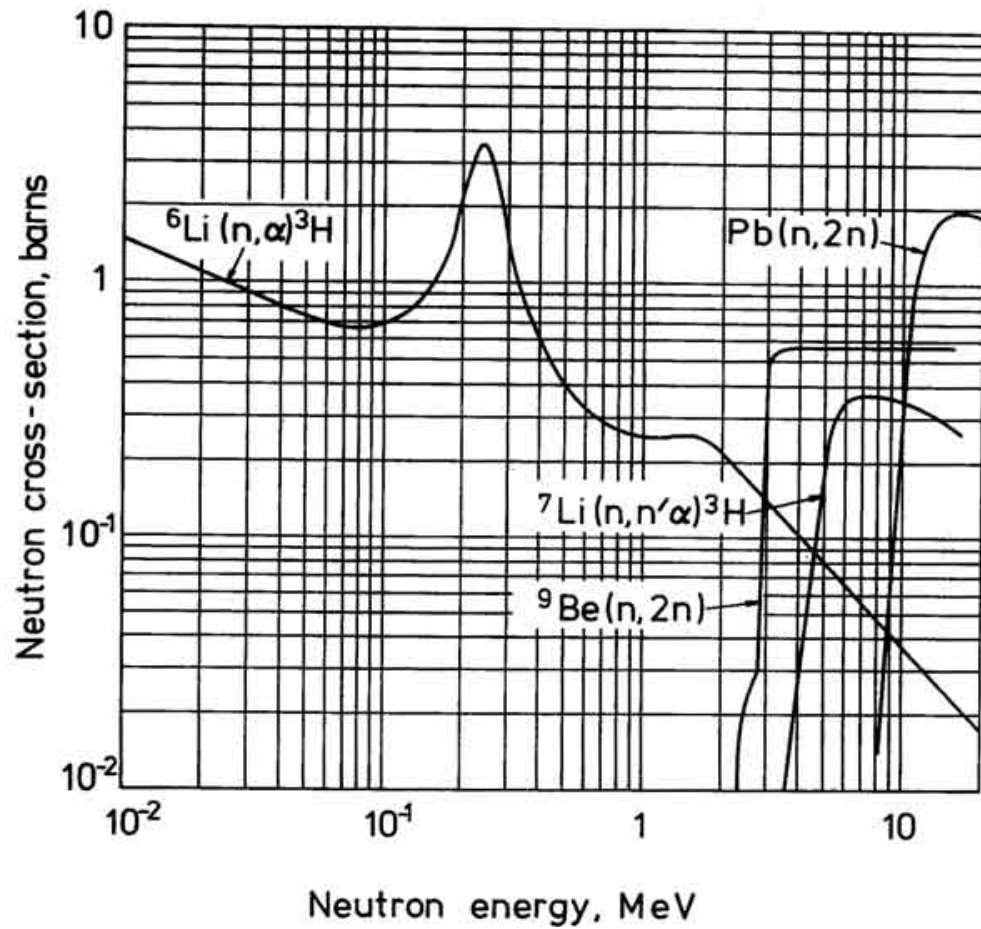


Figure 1.1: Cross-sections of various blanket materials. Note the threshold for the  ${}^7\text{Li}$  and neutron multiplying reactions.

access to abundant supplies of lithium, then if we complete the fuel cycle of neutron-lithium-tritium, we essentially have an inexhaustible energy source.

One classification of the efficacy of a breeding blanket is through the ‘tritium breeding ratio’ of the fusion powerplant, defined as

$$\text{TBR} = \frac{\dot{N}^+}{\dot{N}^-} \quad (1.5)$$

where  $\dot{N}^+$  is the number of tritium atoms generated per unit time and  $\dot{N}^-$  are the number of tritium atoms consumed per unit time.

For a DT cycle,  $\dot{N}^-$  = number of fusion reactions in a plasma per unit time (each fusion reaction produces a single neutron). Therefore, for a DT cycle, we have a simplified definition that the tritium breeding ratio is the number of tritium atoms produced in the blanket per fusion neutron. In order to realize fusion as a commercial energy source, it is utterly crucial that the TBR of the plant design be greater than 1.

Clearly it is essential to engineer a device that surrounds the fusion reaction, captures the ejected neutron to breed tritium, and allows recovery of that tritium to attain self-sufficiency. Additionally, the blanket must also be capable of converting energy deposited from neutrons,  $\gamma$ s, and surface radiation from the plasma and then recovering the energy at high temperatures for efficient power production in the fusion power plant.

Blanket designs have evolved significantly since their introduction in the 1970s. Some features of current breeder designs will be discussed next.

### 1.1.2 Solid breeder design

Reference current styles of design. edge-on, etc.

The solid breeder in many current designs for ITER feature sub-module units of packed beds<sup>1</sup>. From the point of view of pebble bed thermomechanics, this has the advantage of producing units individually that can be tested and qualified to desired packing states (and

therefore thermomechanics) during the design phase.

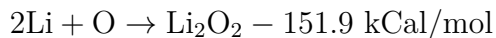
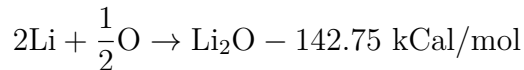
We aim to provide designers of packed beds with tools to understand how packing states may evolve from time-dependent phenomena (e.g. sintering, creep, pebble cracking, etc.). These phenomena may, for instance: decrease the effective thermal conductivity which will raise bed temperatures beyond initial predictions, produce isolated pebbles which will sinter and potentially decrease tritium release rates, or even the form gaps between pebble beds and containing structures leading to divergence from initial packing properties.

### 1.1.3 Material candidates and related phenomena

Lithium can exist in the breeding blanket as either a liquid or a solid. We will limit the scope of our discussion entirely to the solid form. To date, most parties researching solid breeder devices are focusing on lithium orthosilicate ( $\text{Li}_4\text{SiO}_4$ ) or lithium metatitanite ( $\text{Li}_2\text{TiO}_3$ ) as candidate ceramics, though other candidate ceramics do still exist.

Solid breeders are always separately cooled by either water or helium flowing through coolant channels.

Pure lithium is chemically active meaning safety is an issue. As an example, here are two reactions with oxygen along with their heats of formation



note: a negative heat of formation means an exothermic reaction. Lithium will exothermically react with water (or air, concrete, or any moisture-containing materials) with high amounts of energy released. Of primary concern in lithium fires is the peak flame temperature. This will determine, to a large extent, whether many radioactive species become air-borne by vaporization. The flame temperature depends on many variables. Some investigations found it to be about 2500 K which would cause some materials to melt but not vaporize.

## 1.2 Importance of pebble bed integrity and motivation

Control of the manufacturing processes of the ceramic pebbles permits manufactureres to custom vary characteristics, such as the pebble's:

- tritium retention and release properties.
- Lithium density
- Opened- and closed-porosity
- Nominal diameter
- and, indirectly, crush strength.

However the characteristics of the pebble are often coupled. For instance, for the sake of tritium management the open porosity of the pebble is often increased. But this comes at the expense of a decreased crush strength of the pebble. Because of the relatively weak crush strength distributions among batches of pebbles as well as the value of stresses predicted in the pebble bed, it is inevitable that during operation in the fusion environment individual pebbles will ‘fail’ in the ensemble. Designers of lithium ceramic tritium breeding blankets must mitigate pebble failure but also anticipate the breadth and magnitude of effects that some unavoidable failure will have on macroscopic properties.

## 1.3 Scope of the work

To develop a complete numerical model for a pebble bed requires completing many interactive sub-models. To demonstrate, we give here the path of a possible analysis scheme of these models. To begin, one must have knowledge of the interaction of the pebble bed with the containing structure as they exist in a fusion environment. The interactions are generally analyzed via the finite element method to find internal stresses and temperature fields of

the entirety of the pebble bed. After the internal fields are mapped, one would use the discrete element method (DEM) to interpret the macroscopic stress fields into the inter-particle forces. With the inter-particle forces and total absorbed thermal energy calculated, a prediction of the initiation of pebble failure would predict the number of pebbles (if any) that would be crushed in that computational volume. When a pebble is crushed, it loses contact with its neighbors and subsequently breaks any thermal or mechanical transport that the pebble was providing. Fragmentation of a failed pebble would also be handled by the DEM with another model. Following this, DEM would determine how the pebble bed resettles and effective properties evolve in the presence of failed pebbles. Finally, the updated bed properties would feed back into the FEM formulation to predict how overall stress fields and material interactions are altered in light of the failure. The fusion community is far from an integrated simulation that can follow such a path, but it is the principle goal of the overall efforts at UCLA.

Research on pebble failure up to now has focused on predicting when pebbles may fail in a bed as a function of an external load (typically, stress from walls). In this study, we analyze the evolution of pebble bed properties assuming some fraction of pebbles in the ensemble have failed. The focus of this study is to determine the extent of change in aggregate ensemble properties due to individual pebble failure, as well as help designers anticipate acceptable limits of pebble failure from a thermal management point of view. We make use of DEM to simulate individual pebbles in a packed bed. From this scale of simulation, we can study single pebbles undergoing failure while the bed as a whole is subject to mechanical and thermal boundaries.

For the DEM tools used in this study, the only mode of heat transfer is conduction through the solids. In a fusion breeder however, the helium purge gas winding through the interstitial gaps of the pebbles will have a large contribution to overall heat transfer.<sup>?,?</sup> To overcome the current limit on DEM heat transfer, we are also working with computational fluid dynamics coupling to the discrete element method to account for the helium energy transport. The next step is to combine our analysis tools with a failure initiation predictor

as well as a new method of simulating a pebble after failure. Those modeling enhancements will be reported in the future. As these models become more comprehensive in their scope, the fusion community will be better prepared to determine the survivability and performance of a solid breeder design in the fusion environment.

The discrete element method (DEM) is used by many ceramic breeder researchers to model the interaction of individual pebbles in an ensemble in an effort to obtain a more detailed understanding of pebble beds than is possible with experimental measurements of effective properties. For example see Refs.<sup>?, ?, ?, ?, ?, ?</sup> A major assumption in the DEM formulation is that each pebble acts perfectly elastically and adheres to Hertz theory for contacting spheres. With Hertz theory, one finds contact forces as a simple function of: the virtual overlap between two objects, the Young's modulus of the contacting material (and Poisson ratio), and radii of the two. In past studies, the Young's modulus of the ceramic materials used in DEM simulations was taken from historical data, for instance lithium metatitanate from Ref.<sup>?</sup>

Based on observations of experimental data from single pebble crush data, in this study we propose a new method of obtaining the Young's modulus for a batch of ceramic pebbles as the historical values from literature are not always appropriate.

Modeling research on ceramic pebble beds should have as its main objective a thorough understanding of the evolution of pebble bed morphology and the impact on thermophysical properties; allowing for temperature control of breeder pebble beds over the entire lifetime of the blanket. To accomplish that goal, this current study is aimed at developing a methodology for coupling established discrete element models of individual pebbles in the ensemble with thermo-fluid simulations of the interstitial helium purge gas. Specifically, we will address the impact of helium on the thermal transport in a bed experiencing evolving morphology due to cracked pebbles.

Global models of pebble beds and helium flow with pebble-scale detail are intractable with current computational hardware and modeling techniques. To overcome deficiencies in computational power, we introduce two new modeling approaches that allow us to resolve

pebble-scale interactions with bed-scale conjugate heat transfer with flowing gas.

## **Part II**

# **Literature Review**

# CHAPTER 2

## Pebble Interaction Analysis: Theory

In § 5.2, we will lay out the contact interaction mechanics implemented in the discrete element method which include normal and tangential forces and damping. While all the mechanics are important for the fidelity and stability of the DEM simulation, we will focus here purely on the normal elastic contact of two interacting bodies, the analysis which was first performed by Heinrich Hertz in 1882. The results of the so-called Hertzian contact law is vital to many other sections of this work so it is instructive to have the analysis laid out.

### 2.1 Hertz theory for normal contact of spheres

[DRAW SOME COORDINATE DIAGRAMS TO SHOW HOW Z R AND X-Y WHAT-EVER ARE ACTUALLY RELATED AND CAN BE VISUALIZED] We consider two non-conforming solids approaching and then contacting under load. Picture a line connecting the centerpoints of the two bodies and an  $x - y$  plane existing at the midpoint between the bodies and oriented normal to their connecting line. On that surface, there is a radius,  $r$  extending from the connecting line that is related to the  $x - y$  coordinates as  $r^2 = x^2 + y^2$ .

Because we are restricting ourselves to two spheres, the surface of curvature of the two bodies may be written as

$$z_1 = \frac{1}{2R_1}r^2 \quad (2.1a)$$

$$z_2 = \frac{1}{2R_2}r^2 \quad (2.1b)$$

respectively. As the two bodies approach, just before the surfaces are in contact, points on the two surfaces are separated by a distance  $h(r)$ ,

$$\begin{aligned} h &= z_1 - z_2 \\ h &= \left( \frac{1}{R_1} + \frac{1}{R_2} \right) \frac{r^2}{2} \end{aligned} \quad (2.2)$$

Noticing this term in the separation, we define the relative radius of curvature as

$$\frac{1}{R^*} = \frac{1}{R_1} + \frac{1}{R_2} \quad (2.3)$$

and then the separation is simply  $h = (1/2R^*)r^2$ .

The two bodies continue their approach towards each other until finally, under an external load  $F$ , come into contact. The cross-section of these bodies after contact are shown in Fig. 2.1. If we first imagine that the two surfaces do not interact and their surfaces pass through each other unimpeded, their surfaces would be overlapped to a distance  $\delta$ . In such a case, we examine two points deep within the bodies, along the axis of contact, calling them  $T_1$  and  $T_2$ . These points will have moved  $\delta_1$  and  $\delta_2$ , respectively. The total overlap is obviously related to these displacements by  $\delta = \delta_1 + \delta_2$ .

However, under actual interaction, the two surfaces are going to deform as the load  $F$  presses them into contact. So now we consider two points on the surfaces, such as  $S_1$  and  $S_2$ . Before contact, these two points are initially separated by a distance  $h$  (from Eq. 2.2), then displace by  $\bar{u}_{z1}$  and  $\bar{u}_{z2}$  due to contact pressure.

If the points  $S_1$  and  $S_2$  are inside of the contact region under load, these distances are related by

$$\bar{u}_{z1} + \bar{u}_{z2} + h = \delta \quad (2.4)$$

Then using Eq. 2.2, we have an expression for the elastic displacements as

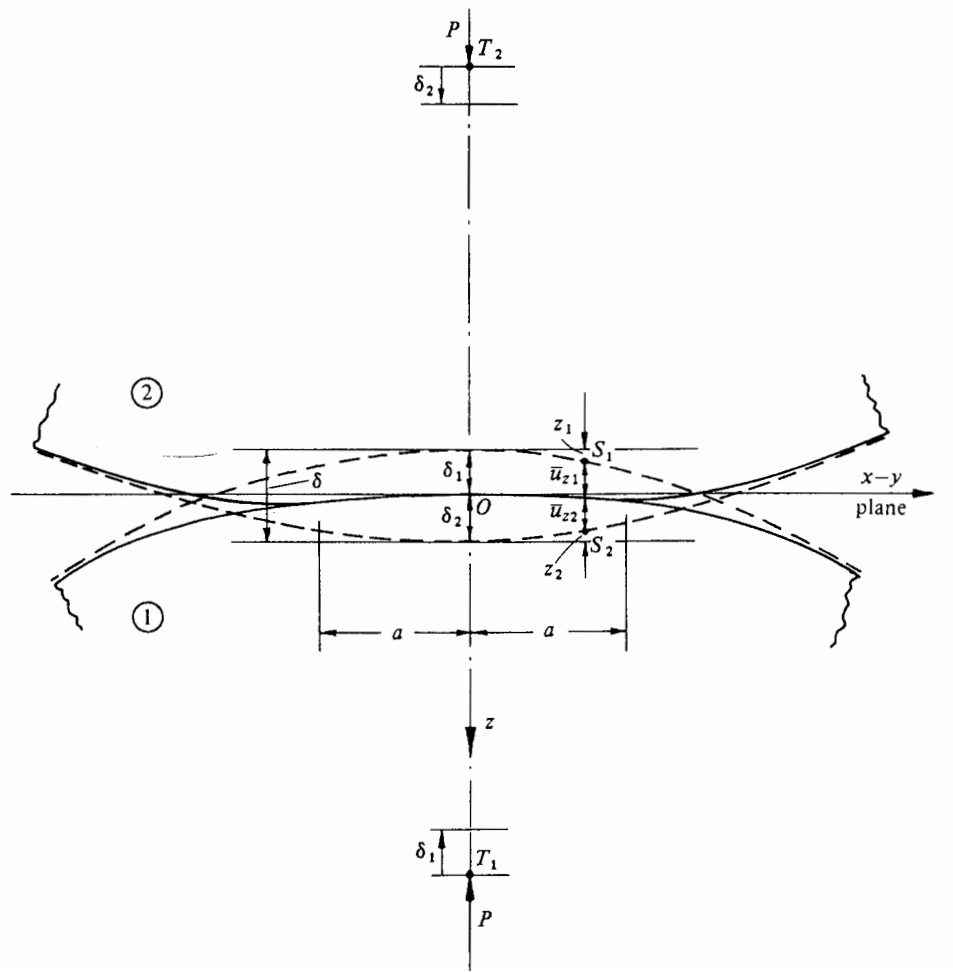


Figure 2.1: default

$$\bar{u}_{z1} + \bar{u}_{z2} = \delta - \frac{1}{2R^*} r^2 \quad (2.5)$$

Alternatively, if after deformation the points  $S_1$  and  $S_2$  are outside of the contact region, this is simply

$$\bar{u}_{z1} + \bar{u}_{z2} > \delta - \frac{1}{2R^*} r^2 \quad (2.6)$$

It now is necessary to find a pressure distribution that satisfies these boundary conditions of displacement. Hertz's great contribution was to simplify the solution of expressions

Eqs. 2.5 and 2.6 by regarding each body as an elastic half-space upon which the load is applied over a small, elliptical region (the contact area). This simplification allows for treatment of the highly concentrated stresses near the region of contact without consideration of either the general response of stresses in the bulk of the body or the manner in which they are supporting the load. This assumption is justifiable if the dimensions of each body as well as the relative radii of curvature are very large compared to the contact area. These assumptions are sufficient to proceed with the analysis, but the curious are pointed to an excellent discussion and background of Hertz's theory as given in KE Johnson's textbook.<sup>?</sup>

For solids of revolution, a distribution of pressure to satisfy the displacements of Eq. 2.6 is proposed by Hertz as

$$p = p_0 \left[ 1 - \left( \frac{r}{a} \right)^2 \right]^{1/2} \quad (2.7)$$

where  $a$  is the radius of the contact area.

The total load,  $F$  is found from the pressure distribution as

$$\begin{aligned} F &= \int_0^a p(r) 2\pi r \, dr \\ F &= \frac{2}{3} p_0 \pi a^2 \end{aligned} \quad (2.8)$$

From the distributed load over the circular region, stresses and deflections are found from superposition of point loads. The pressure is integrated (see Ref.<sup>?</sup>) to find the normal displacement for either solid body as

$$\bar{u}_z = \frac{1 - \nu^2}{E} \frac{\pi p_0}{4a} (2a^2 - r^2) \quad (2.9)$$

This is applied to both bodies and plugged into Eq. 2.5 to yield

$$\frac{\pi p_0}{4a E^*} (2a^2 - r^2) = \delta - \left( \frac{1}{2R^*} \right) r^2 \quad (2.10)$$

where we have introduced the now-common term of pair Young's modulus,

$$\frac{1}{E^*} = \frac{1 - \nu_1^2}{E_1} + \frac{1 - \nu_2^2}{E_2} \quad (2.11)$$

for simplification.

With the solution of Eq. 2.10, if we consider  $r = a$  and  $\delta(a) = 0$ , we find the radius of the contact circle is

$$a = \frac{\pi p_0 R^*}{2 E^*} \quad (2.12)$$

and when  $r = 0$ , we find the overlap as

$$\delta = \frac{\pi a p_0}{2 E^*} \quad (2.13)$$

and alternatively we find the pressure as a function of overlap

$$p_0 = \frac{2 E^* \delta}{\pi a} \quad (2.14)$$

The radius, overlap, and pressure relations are inserted into Eq. 2.8 to find the force (from now on referred to as the Hertz force) as a function of overlap, relative radius, and pair Young's modulus,

$$F = \frac{4}{3} E^* \sqrt{R^*} \delta^{3/2} \quad (2.15)$$

as a last step, to differentiate the force from other terms to be derived later, we specify it as the normal force between sphere  $i$  and sphere  $j$  as

$$F_{n,ij} = \frac{4}{3} E_{ij}^* \sqrt{R_{ij}^*} \delta_{n,ij}^{3/2} \quad (2.16)$$

Equation 2.16 defines the normal contact forces between any two contacting, elastic spheres. This extremely important result acts as the basis of all discrete element method

codes since the concept was first introduced for granular materials by Cundall & Strack in 1979.<sup>7</sup>

It is very appealing to use the Hertz force in a numerical model such as DEM because there are very few assumptions built in to the theory; the material must be elastic and satisfy

$$\frac{a}{R^*} \ll 1 \quad (2.17)$$

In which case the force of Eq. 2.16 is calculated from material and geometric properties alone and no phenomenological, empirical fits are necessary.

## **CHAPTER 3**

### **Pressure drop across packed beds**

# CHAPTER 4

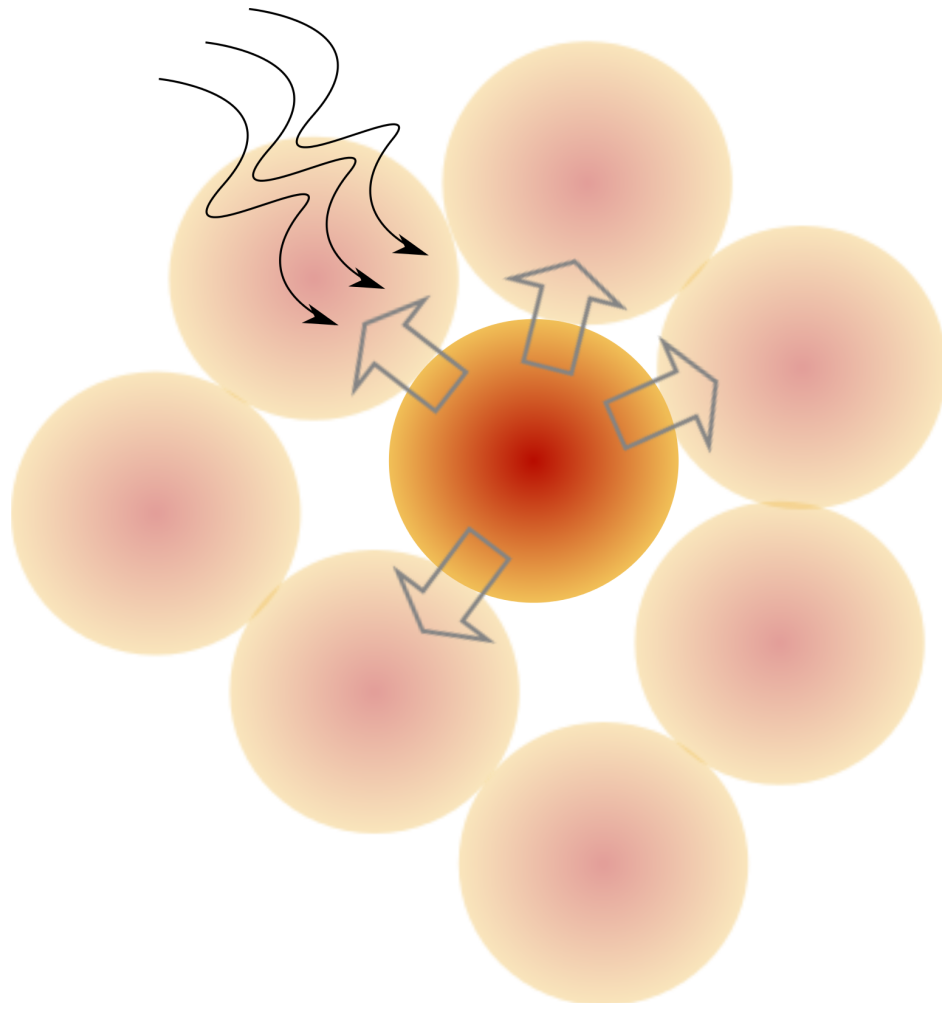
## Heat transfer in packed beds

To begin this section, we begin with a general discussion on the thermal interaction of a single particle inside the packed beds of tritium solid breeders of a fusion reactor. In Fig. 4.1, the different modes of heat transfer are drawn.

1. Conduction through the contact area between contacting particles.
2. Conduction through the stagnant fluid between near, non-contacting particles.
3. Conduction through the stagnant fluid between contacting particles.
4. Conduction through the interstitial fluid.
5. Advection of the fluid to contacting- and downstream particles.
6. Radiation between the surfaces of contacting particles.
7. Radiation between particles of adjacent voids.
8. Heat generation internally in the particle.

The first mode of transfer will be addressed in § 4.1 where we will go through the development of a form of heat conductance between contacting, elastic spheres. Ideally, modes 2-5 would each receive separate treatment but we will wrap up all of their influences with heat transfer coefficients that are functions of local packing fraction to account for both the fluid and the neighboring particles; this is done in § 4.2. For the present study, we will entirely neglect the modes 6, and 7 because of their added complexity. Finally, the last mode of heat transfer is trivially accounted for with a heat source term,

Figure 4.1: Each ceramic pebble in a fusion reactor will experience multiple modes of heat transfer.



$$Q_g = q''V \quad (4.1)$$

where  $q''$  is a known volumetric heating rate and  $V$  is the volume of our particle. In practice, we will know a volumetric heating rate from the location and geometry of the solid breeder volume. The volume of the sphere is  $V = \frac{4}{3}\pi R^3$ .

In the following sections we will expand upon the details of the modes of heat transfer considered for our packed beds. They forms of equations used will be written in a way to be implemented directly into the DEM computational framework, to be discussed later in § 5.

## 4.1 Inter-particle heat conduction

When two particles come into contact, energy is transmitted through their region of contact. For this discussion, we assume the particles are spherical, elastic, in vacuum, and we neglect radiation transfer between them. The resistance to heat flowing between the two objects is quantified through a contact conductance,  $H_c$ . The amount of energy passing between the two particles (labeled  $i$  and  $j$ ) is then

$$Q_{ij} = H_c(T_i - T_j) \quad (4.2)$$

where each contacting pair has a specific value of  $H_c$ . We note that the heat conductance, unlike standard heat transfer coefficients, has units of W/K.

Batchelor and O'Brien<sup>7</sup> developed a formulation of similar form and then made the brilliant observation that the temperature fields in the near-region of contacting spheres are analogous to the velocity potential of the an (incompressible, irrotational) fluid passing from one reservoir to another through a circular hole in a planar wall separating the two reservoirs. With the analogy, they could make use of the fluid flow solution to write the total flux across the circle of contact as Eq. 4.2 with the heat conductance as

$$H_c = 2k_r a = 2k_r \left( \frac{3}{4} \frac{R^*}{E^*} \right)^{1/3} F^{1/3} \quad (4.3)$$

where  $k_r$  is the conductivity of the contacting solids and  $a$  is the radius of contact. In § 2.1, with Hertz theory we found the contact radius in terms of the contact pressure. Here, we give the radius in terms of the compression force acting on the bodies,

$$a = \left( \frac{3}{4} \frac{R^*}{E^*} \right)^{1/3} F_n^{1/3} \quad (4.4)$$

as before,  $\frac{1}{E^*} = \frac{1-\nu_1^2}{E_1} + \frac{1-\nu_2^2}{E_2}$  and  $\frac{1}{R^*} = \frac{1}{R_1} + \frac{1}{R_2}$ .

In Eq. 4.3, Batchelor and O'Brien had assumed the two contacting spheres to be of equal conductivity,  $k_r$ . Cheng, et al.<sup>7</sup> proposed a slightly modified conductance which allows for

contacting materials of different thermal conductivity. They have,

$$H_c = 2k^*a = 2k^* \left( \frac{3}{4} \frac{R^*}{E^*} \right)^{1/3} F_n^{1/3} \quad (4.5)$$

where  $\frac{1}{k^*} = \frac{1}{k_i} + \frac{1}{k_j}$ . As well as being a more general, flexible formulation, the models analyzed by Cheng, et al.<sup>7</sup> are in good agreement with experiments. In the DEM numerical structure, we use the form given by Eq. 4.5.

Batchelor and O'Brien developed Eq. 4.3 with the assumption of two contacting particles in vacuum but, once developed, showed<sup>7</sup> that this form is still valid when immersed in a fluid providing that the thermal conductivity ratio of solid and fluid is well above unity. The condition is expressed as,

$$\frac{k_r}{k_f} \frac{a}{R^*} \gg 1 \quad (4.6)$$

The term  $\frac{a}{R^*}$ , from § 2.1, is necessarily much less than 1 for Hertz theory to be applicable. Thus for fluid in vacuum, the condition is identically satisfied but we must consider inaccuracies if we introduce an interstitial fluid with low conductivity ratios.

For lithium ceramics in helium, the ratio is approximately  $\frac{k_r}{k_f} \approx 10$  which is not necessarily large enough to satisfy the requirement of Eq. 4.6.

As we step back from the contact of a single pair of particles and consider a particle in an ensemble with many contacts, we must again consider the validity of applying Eq. 4.5 at each contact. Vargas and McCarthy,<sup>7</sup> proposed introducing a conduction Biot number to relate resistance to heat transfer internal to the particle with the resistance between particles. We use the following form

$$\text{Bi}_c = \frac{H_c}{k^* d_p} = 2 \frac{a}{d_p} \quad (4.7)$$

Then if  $\text{Bi}_c \ll 1$ , the individual energy transferred between each point of contact can be decoupled. The Biot number criteria is already satisfied for Hertz theory to be valid; having

assumed that  $\frac{a}{d_p} \ll 1$ . Therefore the total heat transferred out of a single particle with  $Z$  contacts is summed from the individual contacts as

$$Q_i = \sum_j^Z Q_{ij} \quad (4.8)$$

The form of contact conductance used in our study, built upon the solution of Batchelor and O'Brien,<sup>7</sup> has been implemented by others in a variety of studies.<sup>?, ?, ?, ?</sup> However, in many other fields, the researchers are interested in such things as the parallel conduction through a stagnant interstitial gas<sup>7</sup> or the temporary conduction during impact of fluidized beds.<sup>?, ?, ?, ?</sup>

Nevertheless, for the packed beds of ceramic spheres we intend to model, the heat conductance of Eq. 4.5 is an appropriate and valid form. When we incorporate the influence of an interstitial gas, it will be done in such a way as to leave the DEM heat transfer intact and only add an energy source term to stand in for the interaction with the fluid. The details will be discussed in § 6.1.1, but for now we conclude with a solid conduction theory that will be implemented in the discrete element method computations.

## 4.2 Nusselt number for spheres in packed beds

Historically, in the treatment of packed beds for heat transfer, engineers developed relationships between overall heat transfer coefficients to the log-mean temperature of the bed. The Nusselt number correlation was applicable to the bed overall rather than any discrete particle inside of the bed. The correlations will be useful for validating our models of helium flow through packed beds of lithium ceramics.

Recently, however, experimental and numerical research has focused on the heat transfer at the scale of a particle as a component of dilute or dense packed beds. These correlations will be useful for applying to single discrete elements in our DEM framework.

$$Q_{\text{convection}} = -hA_r(T_r - T_f) \quad (4.9)$$

where  $T_r$  is the temperature of the solid with surface area,  $A_r$ , and  $T_f$  is the local bulk temperature of the passing fluid.

#### 4.2.1 Packed bed correlations: Nellis and Klein

A heat transfer coefficient for a packed bed of spheres, as given by Nellis and Klein, is determined strictly on geometric details of the packed bed. Necessary values are the porosity, or void fraction,  $\epsilon$ , and the cross-sectional surface area of the bed,  $A_t$ .

The average heat transfer coefficient is correlated in terms of the Colburn  $j_h$  factor.

$$j_h = \frac{\bar{h}}{GC_f} \text{Pr}^{2/3} \quad (4.10)$$

The mass flux,  $G$ , is evaluated in terms of the specific surface area and mass flow rate:

$$G = \frac{\dot{m}}{\epsilon A_t} \quad (4.11)$$

where  $C_f$  is the specific heat capacity of the fluid and  $\text{Pr}$  the Prandtl number of the fluid. For a packed bed of spheres, Nellis & Klein used the modified Reynolds number suggested by Kays and London (1984), defined as,

$$\text{Re}_G = \frac{4Gr_{char}}{\mu_f} \quad (4.12)$$

where  $\mu_f$  is the viscosity of the fluid. The characteristic radius  $r_{char}$  is given as:

$$r_{char} = \frac{\epsilon d_p}{4(1 - \epsilon)} \quad (4.13)$$

where  $d_p$  is the average diameter of the packed bed particle. The relationship between Colburn  $j_h$  factor and mass-flux Reynolds number was provided in Nellis and Klein. The interpolation of their data yields a functional relationship of,

$$jh = 0.191 \text{Re}_G^{-0.278} \quad (4.14)$$

Therefore, the heat transfer coefficient is found as,

$$h = (0.191 \text{Re}_G^{-0.278}) \left( \frac{\dot{m}}{\epsilon A_t} \right) C_f Pr^{-2/3} \quad (4.15)$$

which is applicable for spherical objects in densely packed beds.

#### 4.2.2 Packed beds correlation: Whitaker

Definition of Reynolds number

$$\text{Re} = \frac{D_p G}{\mu_b (1 - \epsilon)} \quad (4.16)$$

Definition of Nusselt number

$$\text{Nu} = \frac{h D_p}{k_f} \frac{\epsilon}{1 - \epsilon} \quad (4.17)$$

Definition of h

$$h_{\ln} = \frac{\dot{Q}}{a_v} V \Delta T_{\ln} \quad (4.18)$$

where  $a_v = (A_p/V_p)(1 - \epsilon)$  is the surface area per unit volume. And  $\Delta T_{\ln}$  is the log-mean temperature difference.

Reference temp,  $T^*$

$$T^* = \frac{1}{2} (T_{f1} + T_{f2}) \quad (4.19)$$

Range of Reynolds number  $22 - 8 \times 10^3$

Range of Prandtl number 0.7

Range of  $(\mu_b/\mu_0)$  1

Correlation,

$$\text{Nu} = \left(0.5\text{Re}^{1/2} + 0.2\text{Re}^{2/3}\right) \text{Pr}^{1/3} \quad (4.20)$$

#### 4.2.3 Single pebble correlations

For a sphere in an infinite, quiescent fluid where conduction is the only mode of heat transfer, the Nusselt number is identically 2. In all the single particle correlations, that value is the limit as  $\text{Re} \rightarrow 0$ .

Ranz & Marshall in 1952

Zhou, et al 2009

$$\text{Nu}_i = 2.0 + 1.2\text{Re}_i^{1/2} \text{Pr}^{1/3} \quad (4.21)$$

### 4.3 Jeffreson correction to lumped capacitance method

In § 4.2, we discuss correlations for heat transfer coefficients of spheres in a packed bed. Then those correlations are utilized with CFD-DEM computational routines in eq. (6.2). When implemented in the DEM-based modeling, we make the lumped capacitance assumption for each particle in the ensemble. The assumption eases the computational efforts of solving for the temperature distribution inside each particle; each particle is treated as isothermal. The accuracy of the lumped capacitance method is described by the Biot number,

$$\text{Bi} = \frac{hd_p}{k_r} \quad (4.22)$$

and for  $\text{Bi} \ll 1$  the lumped capacitance method accurately models the behavior of a solid

interacting with a fluid. For  $\text{Bi} \approx 0.1$ , the error from the lumped capacitance method is only about 5%. In solid breeder volumes, the particles are generally small, solid conductivity low, and heat transfer coefficient generally also low. This leads to small-to-moderate Biot numbers expected in the packed bed. In this section we will analyze the accuracy of the lumped capacitance and introduce a correction method to account for inaccuracies of the method at moderate Biot numbers.

We simplify the case of a packed bed and only consider a single sphere with volumetric heat generation submerged in and thermally interacting with a fluid. The sphere will be of radius  $R = d_p/2$ , as shown in Fig. 4.2. The sphere will initially be at a uniform temperature of  $T_i$ . The fluid temperature will remain constant at  $T_f$

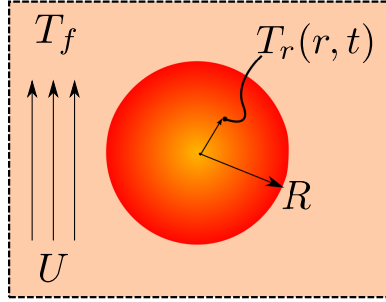


Figure 4.2: CONTROL VOLUME OF A SINGLE SPHERICAL PARTICLE IN A PACKED BED

#### 4.3.1 Lumped capacitance solution for sphere

We will solve for a single sphere interacting with a passing fluid, as shown in Fig. 4.2. We make the lumped capacitance assumption for this sphere. The solid is initially at temperature  $T_0$ , with constant volumetric heat generation, cooling in a fluid with constant heat transfer coefficient. The fluid will remain constant at  $T_f$ .

The time response of the sphere's temperature is dictated by the balance of energy to/away from the solid,

$$\rho_r C_r V \frac{dT}{dt} = -hA(T - T_f) + gV \quad (4.23)$$

Eq. 4.23 is solved in dimensionless form with the following nondimensional parameters of temperature and time,

$$\theta = \frac{T(t) - T_f}{T_0 - T_f} \quad (4.24a)$$

$$\tau = \frac{t}{R^2/\alpha} \quad (4.24b)$$

where  $\alpha$  is the thermal diffusivity of the sphere,  $T_0$  is the initial isothermal temperature of the sphere, and  $T_f$  is the constant fluid temperature. The resulting temperature distribution is,

$$\theta_{LC} = \left(1 - \frac{G}{3Bi}\right) \exp(-3Bi\tau) + \frac{G}{3Bi} \quad (4.25)$$

where we define a dimensionless heat generation,

$$G = \frac{gR^2}{k(T_0 - T_f)} \quad (4.26)$$

The energy of the sphere, relative to the fluid, in nondimensional terms is

$$E^*(\tau) = \frac{E(\tau)}{E_0} \quad (4.27)$$

where  $E_0$  is the initial energy of the sphere,

$$E_0 = \rho_r C_r V (T_0 - T_f) \quad (4.28)$$

Thus for a sphere with the lumped capacitance model, in nondimensional form, is simply

$$E_{LC}^*(\tau) = \theta_{LC}(\tau) \quad (4.29)$$

The nondimensional energy profile of Eq. 4.29 is plotted over the nondimensional time of  $\tau \in [0, 1/\text{Bi}]$  in Fig. 4.3.

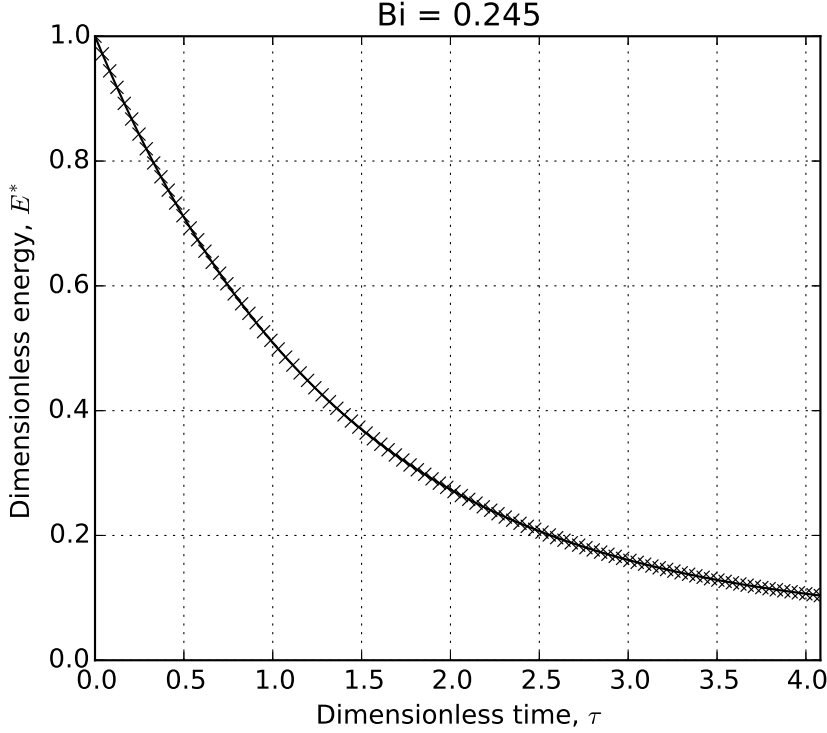


Figure 4.3: Lumped capacitance model: Sphere energy profile decaying from an initial value to a time of  $1/\text{Bi}$

Reviewing Eq. 4.25 we see that the speed of decay is dictated by the term in the exponential,  $3\text{Bi}$ . Meanwhile, the steady-state value being approached is given by  $\frac{G}{3\text{Bi}} = \frac{gR}{h(T_0 - T_f)}$ . It is important for this discussion to point out that because both the nondimensional heat generation and Biot number terms contain the solid conductivity, the steady-state value of the lumped capacitance model will not change for varying solid conductivity even if it leads to different Biot numbers. We will return to this point in the next section when we compare the lumped capacitance model to the exact solution when internal conduction of the solid is considered.

### 4.3.2 Exact solution for sphere

We again analyze the sphere of Fig. 4.2 but now will account for internal temperature gradients inside the sphere. The details of the analytic solution for a sphere with heat generation interacting with a fluid is given in Appendix A. We again solve in terms of the nondimensional temperature and time introduced in § 4.3.1 as well as a nondimensional radius,

$$\begin{aligned}\theta &= \frac{T}{T_0} \\ \rho &= \frac{r}{R} \\ \tau &= \frac{t}{R^2/\alpha}\end{aligned}$$

The energy conservation equation for the sphere with internal temperature gradient, in nondimensional form  $\theta_{TG}$ , is

$$\frac{1}{\rho} \frac{\partial^2}{\partial \rho^2} (\rho \theta_{TG}) + G = \frac{\partial \theta_{TG}}{\partial \tau} \quad (4.30)$$

With the initial condition and boundary conditions outlined in Appendix A, the nondimensional temperature distribution inside the sphere is

$$\theta_{TG}(\rho, \tau) = \left( \frac{G}{6} + \frac{G}{3Bi} - \rho^2 \right) + \sum_{n=1}^{\infty} \exp(-\zeta_n^2 \tau) \frac{\sin(\zeta_n \rho)}{\rho} \frac{Z(\zeta_n)}{N(\zeta_n)} \quad (4.31)$$

where  $\zeta_n$  are the eigenvalues of the equation and the functions of  $\zeta_n$  ( $Z, N, C$ ) are given in Appendix 4.3.2.

The accompanying nondimensional energy of the sphere is integrated to,

$$E_{TG}^*(\tau) = \left( \frac{G}{15} + \frac{G}{3Bi} \right) + 3 \sum_{n=1}^{\infty} \exp(-\zeta_n^2 \tau) \frac{Z(\zeta_n)}{N(\zeta_n)} C_n(\zeta_n) \quad (4.32)$$

We now compare the exact solution from Eq. 4.32 to the solution of energy given by the lumped capacitance model of Eq. 4.29. The two profiles are given in Fig. 4.4.

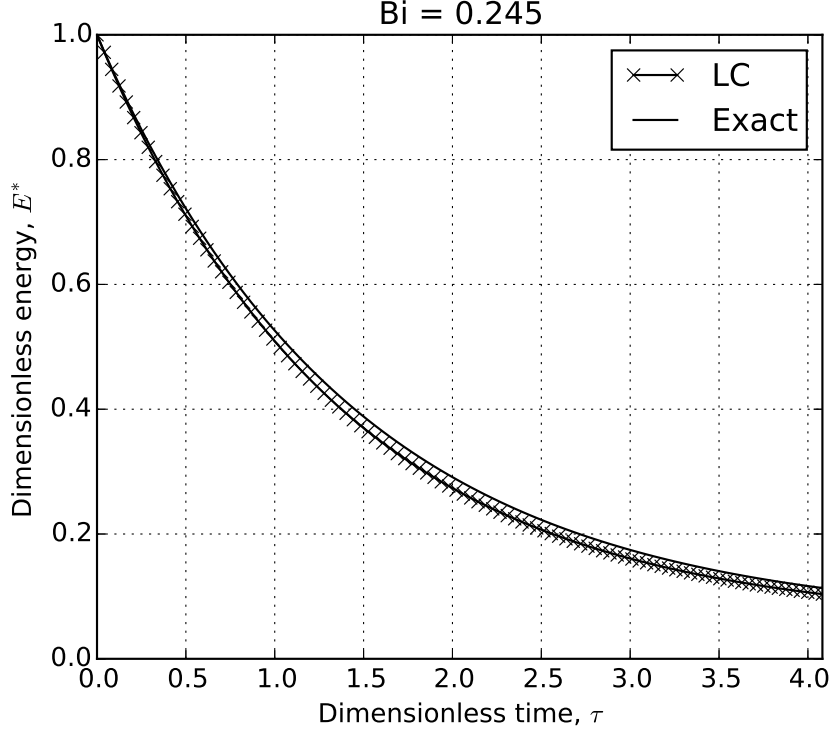


Figure 4.4: Analytic and lumped capacitance models: Sphere energy profile decaying from an initial value to a time of  $1/\text{Bi}$

For the value of Biot number here,  $\text{Bi} < 0.5$ , the profile of the analytic solution of the sphere is well-captured by the lumped capacitance model. The maximum relative error over the time span, as defined by

$$\text{error} = \frac{|E_{TG}^*(\tau) - E_{LC}^*(\tau)|}{E_{TG}^*(\tau)} \quad (4.33)$$

is always less than 10%.

We consider now the same size sphere but with the Biot number increased by an order by: a) a conductivity of  $k = k_r/10$  and b) a heat transfer coefficient of  $h = 10h_f$ . The two physical changes to the system result in the same Biot number but as we can see in Fig. 4.5,

there are drastic changes in the results.

Seen in Fig. 4.5a, the lumped capacitance solution both over-predicts the speed at which the sphere reaches a thermal steady-state as well as the value of the steady-state. Comparatively, in Fig. 4.5b, for the same Biot number the lumped capacitance solution again over-predicts the speed to thermal steady-state by the same rate but is relatively accurate for the steady-state value itself.

To first address the source of error on the steady-state value, we view the steady-state terms of the two solutions. From Eq. 4.32, we write the steady-state term of the exact solution as

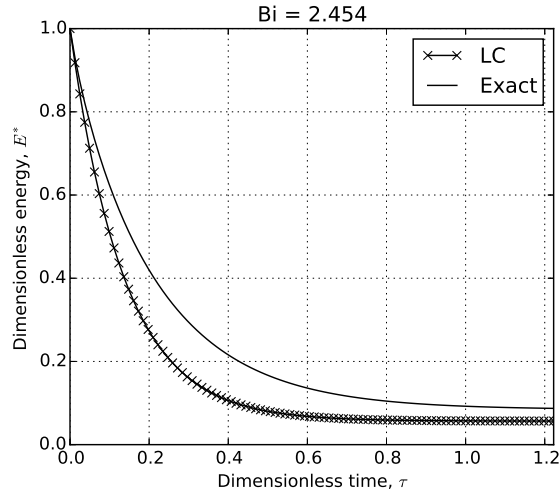
$$E_{TG,ss}^* = \frac{G}{15} + \frac{G}{3Bi} \quad (4.34)$$

Comparatively, we write the steady-state term of the lumped capacitance solution from § 4.3.1 as,

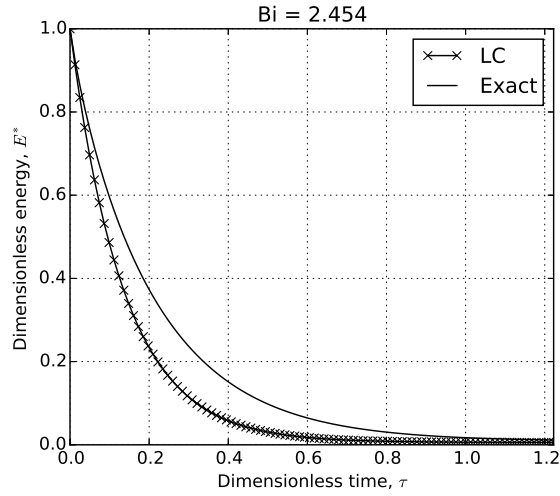
$$E_{LG,ss}^* = \frac{G}{3Bi} \quad (4.35)$$

We clearly see that the two steady-state values differ by the contribution of  $\frac{G}{15}$  on the exact solution. This term does not appear in the lumped capacitance solution because it does not account for the temperature difference through the sphere. The nondimensional heat generation term is given in Eq. 4.26; it is importantly a function of thermal conductivity but not the heat transfer coefficient. This explains the difference between steady-state values in Fig. 4.5 when we modified the two parameters.

To address the inaccuracies in the time-dependent response of the lumped capacitance method with large Biot number, we will make use of the so-called Jeffreson Correction described by Van Lew<sup>7</sup> and Xu et al.<sup>8</sup> In their work, they considered a heated heat transfer fluid interacting with a low conductivity thermal storage material. The solar thermal storage systems they analyzed often had moderate-to-large Biot numbers but they could continue to apply the lumped capacitance model by applying the Jeffreson Correction.<sup>9</sup> The details



(a) The Biot number increased from a decrease in the solid conductivity.



(b) The Biot number increased from an increase in the heat transfer coefficient.

Figure 4.5: Analytic and lumped capacitance models: Sphere energy profile decaying from an initial value to a time of  $3/Bi$ . The same Biot number produces different results for the exact solution of a sphere with heat generation.

of the Jeffreson correction as applied to a system with volumetric heat generation will be discussed next.

### 4.3.3 Jeffreson correction for sphere

In Fig. 4.5, the lumped capacitance model predicted a much faster decay to steady-state than the exact solution. Jeffreson summarized a correction to the lumped capacitance model via a reduction in the heat transfer coefficient as a function of the Biot number. The smaller heat transfer coefficient effectively slowed the decay to steady-state as predicted by the lumped capacitance method. The correlation to correct the heat transfer coefficient due to solids with large Biot number is given by Jeffreson.<sup>7</sup> The Jeffreson correction for a sphere is,

$$h_p = \frac{h}{1 + Bi/5} \quad (4.36)$$

where  $h_p$  is the modified heat transfer coefficient of the particle with an internal temperature gradient. An increase in the Biot Number (or increase of thermal gradient inside the solid) results in a decrease in the heat transfer coefficient  $h_p$ . A modified Biot number can then also be written as

$$Bi_p = \frac{h_p d}{k_r} = \frac{Bi}{1 + Bi/5} \quad (4.37)$$

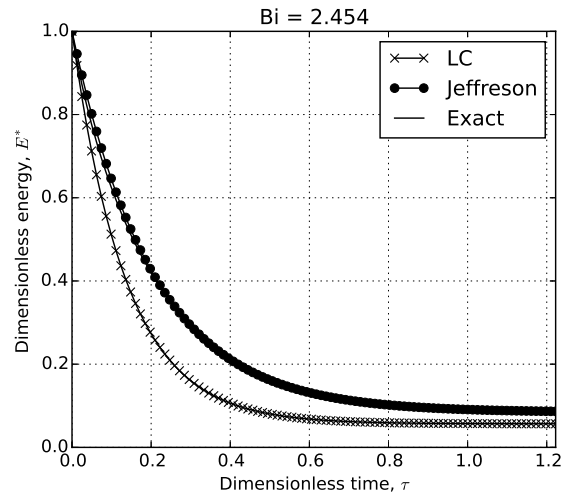
Applying the Jeffreson Correction to Eq. 4.25,

$$\theta_{JC} = \left(1 - \frac{G}{3Bi_p}\right) \exp(-3Bi_p\tau) + \frac{G}{3Bi_p} \quad (4.38)$$

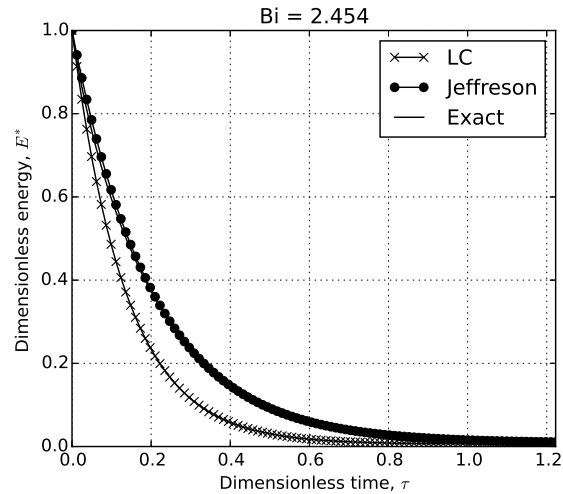
and thereby Eq. 4.29 gives

$$E_{JC}^*(\tau) = \theta_{JC}(\tau) \quad (4.39)$$

We then plot the energy profiles from the lumped capacitance model (LC), the Jeffreson correction (JC), and the exact solution together in Fig. 4.6



(a) The Biot number increased from a decrease in the solid conductivity.



(b) The Biot number increased from an increase in the heat transfer coefficient.

Figure 4.6: Analytic, lumped capacitance model, and LC model with Jeffreson correction: Jeffreson correction corrects for transient and steady-state errors of lumped capacitance.

The Jeffreson correction to the lumped capacitance method allows the simple model to capture the proper transient as well as steady-state values for this sphere with a moderately sized Biot number. To look more closely, we view the instantaneous error (see Eq. 4.33) in Fig. 4.7.

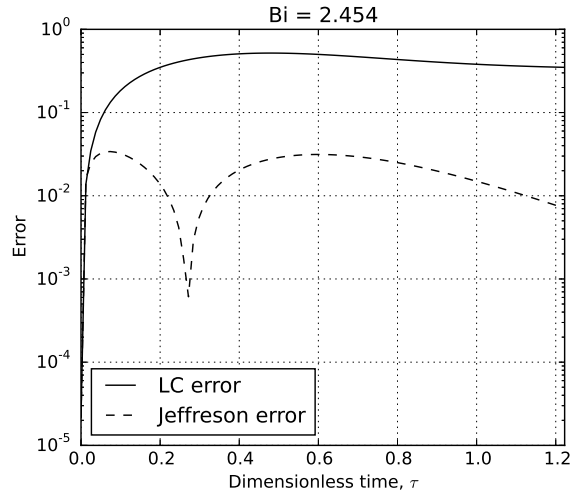
For the value of  $\text{Bi} > 1$  due to either low conductivity (Fig. 4.7a) or high heat transfer coefficient (Fig. 4.7b), the error in the Jeffreson correction is always under 10%; often closer to only 1%. This is in opposition to the standard lumped capacitance method which has 50-80% error for both transient and steady-state values.

The lumped capacitance method allows researchers to simplify transient, conjugate heat transfer problems with an isothermal solid. In the discrete element method, the assumption of isothermal solid is innate in the framework of the method. With the implementation of the Jeffreson correction in the discrete element method, we have confidence in the fidelity of the heat transfer in for moderately sized Biot numbers. The Jeffreson correction will be implemented into the DEM computations via Eq. 4.37.

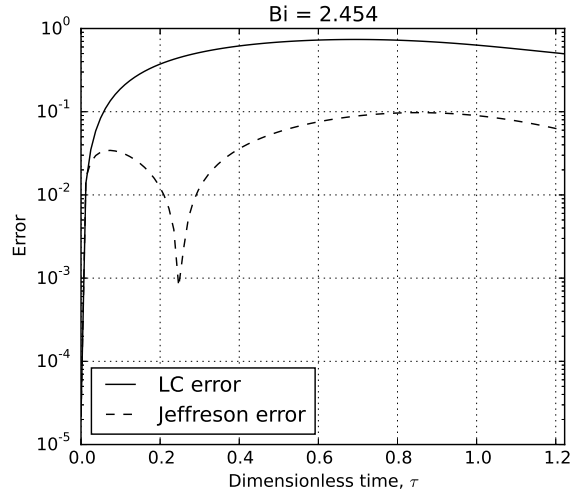
## 4.4 Radiative transfer with neighboring particles

The temperatures expected in the solid breeder are high enough that we can not a priori neglect radiation. The radiation exchange between contacting neighbors in a packed bed becomes extremely complex due to the local and semi-local nature of radiation. A standard approach to treat radiation exchange between surfaces is to consider the view factor between them. In a dense, randomly packed bed of spheres the computation of view factors between pebbles can be done via a method such as that proposed Feng and Han.<sup>7</sup> Ideally, we could show this mode of heat transport is negligible compared to the others already discussed.

In ceramic breeder designs, the tritium breeding volume is rarely more than 2 cm wide with pebbles that are, generally, 1 mm in diameter. The maximum expected temperature in the breeding zone is about 1000 K, roughly at the centerline of the 2 cm width. The walls of the coolant must be held below the operable steel temperature of roughly 700 K. This



(a) The Biot number increased from a decrease in the solid conductivity.



(b) The Biot number increased from an increase in the heat transfer coefficient.

Figure 4.7: Error of lumped capacitance and reduced error of the model with Jeffreson correction for moderate Biot number.

works out to a 300 K differences spanning 10 pebble diameters. From this we can make a first-order approximation of 30 K difference between neighboring pebbles. At the elevated temperatures, an estimate for the radiation exchange between two pebbles (allowing them to act as black bodies for this approximation) is

$$\dot{Q}_{\text{radiation}} = \sigma A (T_{\max}^4 - (T_{\max} - 30)^4) \approx 0.022 \text{W} \quad (4.40)$$

which is the highest amount of radiation exchange we might expect between pebbles. Even though we will neglect this mode of heat transfer for now, after reviewing some of the packed bed heat transfer results we may find that this quantity of energy transfer is not negligible and future versions of the model would have to account for it.

Part III

## Methodology

# CHAPTER 5

## Modeling Discrete Element Method (DEM)

This chapter presents the motivations and background of this study. First, it discusses energy usage in our society and the inevitable production of waste mechanical and thermal energies and their ubiquitous nature. This is followed by a brief discussion of common methods of converting ambient mechanical energy and waste heat into useful electrical energy. This chapter concludes with the objectives of this study and the scope of the document.

### 5.1 Background

The observable, macroscopic behavior of particulate, or granular, systems is a complex function of the multitude of particle-scale interactions. Historically, empirical relationships have been used to describe these systems as if a continuous media. But with the advent of the discrete element method by Cundall and Strack<sup>7</sup> and the acceleration of computing power, it became practical to investigate these particulate systems at the particle scale. With the discrete element method, we track all the particles in the system in a Lagrangian manner. In the ensemble, the kinematics of each particle is tracked and updated based on balances (or imbalances) of forces or energy acting upon the particle.

Experiments on packed beds are generally limited to measurements of statistically averaged, macroscopic responses. Unlike continuous materials, packed beds as yet can not be described by any State. For instance, with an ideal gas if we know two properties such as temperature or pressure, the State of the gas is known and its behavior predicted. Two packed beds with the same temperature, packing fraction, average particle diameter, and stress state may react wildly different. As researchers we create empirical fits to data on

the particular packed bed under investigation but then might have to dubiously apply the relationships to beds of different packing states.

DEM is emerging as a reliable method to remove speculation about the internal state of the packed bed as the simulations provide valuable information on the dynamics of particle interactions and how they relate to the macroscopic responses that are measured experimentally.

In this chapter we will lay out the formulas governing interaction of particles in the DEM framework, the methods of computation, and the code used for implementation. In § 5.4, we will use the derivation of the Hertz contact law described in § 2 to argue for a technique of accelerating the computational time without loss of physics via proper scaling of physical parameters. Lastly, in § 8.1, we use our DEM tools to investigate the thermo physics of representative packed beds for solid breeders in fusion reactors.

## 5.2 Particle dynamics

The particles in our system are allowed translational and rotational degrees of freedom. In a packed bed, we can restrict our attention to local forces between particles; neglecting, say, non-contact forces such as van der Waals or electrostatic forces. In the first construct, we will treat the particles as if in a vacuum and leave a derivation of fluid interaction forces for § 6.

### 5.2.1 Particle kinematics

Assuming we know the contact forces acting upon particle  $i$ , Newton's equations of motion describe the motion of the particle. The translational and rotational for the translation degrees of freedom:

$$m_i \frac{d^2 \mathbf{r}_i}{dt^2} = m_i \mathbf{g} + \mathbf{f}_i \quad (5.1a)$$

$$I_i \frac{d\omega_i}{dt} = \mathbf{T}_i \quad (5.1b)$$

where  $m_i$  is the mass of this particle,  $\mathbf{r}_i$  its location in space,  $\mathbf{g}$  is gravity,  $I_i$  is the particle's moment of inertia, and  $\omega_i$  its angular velocity.

The net contact force,  $\mathbf{f}_i$ , represents the sum of the normal and tangential forces from the total number of contacts,  $Z$ , acting on this particle.

$$\mathbf{f}_i = \sum_{j=1}^Z \mathbf{f}_{n,ij} + \mathbf{f}_{t,ij} \quad (5.2)$$

and the net torque,  $\mathbf{T}_i$ , is similarly,

$$\mathbf{T}_i = -\frac{1}{2} \sum_{j=1}^Z \mathbf{r}_{ij} \times \mathbf{f}_{t,ij} \quad (5.3)$$

### 5.2.2 Linear spring-dashpot model

When Cundall and Strack first proposed the discrete element method, they used a linear spring-dashpot structure which saw the normal and tangential forces written as,

$$\mathbf{f}_{n,ij} = k_{n,ij} \delta_{n,ij} \mathbf{n}_{ij} - \gamma_{n,ij} \mathbf{u}_{n,ij} \quad (5.4a)$$

$$\mathbf{f}_{t,ij} = k_{t,ij} \delta_{t,ij} \mathbf{t}_{ij} - \gamma_{t,ij} \mathbf{u}_{t,ij} \quad (5.4b)$$

The fictive tangential overlap,  $\delta_{t,ij}$ , is truncated to so the tangential and normal forces obey Coulomb's Law,  $\mathbf{f}_{t,ij} \leq \mu_i \mathbf{f}_{n,ij}$  with  $\mu$  as the coefficient of friction of the particle. In the first model of Cundall and Strack, the stiffness coefficients  $k$  were constants and the local damping coefficients  $\gamma$  were proportional to them,  $\gamma \propto k$  to allow dissipation of energy

and the system to reach an equilibrium. The relative normal and tangential velocities, respectively, are decomposed from the particle velocities,

$$\mathbf{u}_{n,ij} = (-(\mathbf{u}_i - \mathbf{u}_j) \cdot \mathbf{n}_{ij}) \mathbf{n}_{ij} \quad (5.5a)$$

$$\mathbf{u}_{t,ij} = (-(\mathbf{u}_i - \mathbf{u}_j) \cdot \mathbf{t}_{ij}) \mathbf{t}_{ij} \quad (5.5b)$$

with the unit vector  $\mathbf{n}_{ij}$  pointing from particle  $j$  to  $i$

Similarly to the approach of Hertz (see § 2), the surfaces of the two particles are allowed to virtually pass through each other (no deformation) resulting in normal and tangential overlaps of,

$$\delta_{n,ij} = (R_i + R_j) - (\mathbf{r}_i - \mathbf{r}_j) \cdot \mathbf{n}_{ij} \quad (5.6a)$$

$$\delta_{t,ij} = \int_{t_{c,0}}^t \mathbf{u}_{t,ij} d\tau \quad (5.6b)$$

We have a relatively simple approach of calculating the interaction forces between particles with Eq. 5.4 based on the kinematics of velocity and position of the interacting particles from Eq. 5.5 and Eq. 5.6, respectively. As the DEM evolved and drew the attention of more researchers, more complex formulas governing the forces of Eq. 5.4 emerged. But the core approach remained the same and the models all fall into the same family of so-called ‘soft particle’ models of DEM. A well-composed summary of the different DEM force models is given by Zhu et al.<sup>?</sup>

The method used in our work is fit into the computational skeleton of Cundall and Strack’s method but with non-linear spring-dashpot coefficients defined by simplified Hertz-Mindlin-Deresiewicz model; the details will be expressed in the next section.

### 5.2.3 Hertzian non-linear spring dashpot model

The normal-direction (Hertz) stiffness coefficient of Eq. 5.4a is based on the Hertzian contact laws given in § 2.1. The tangential-direction (Mindlin) stiffness coefficient follows from Brilliantov <sup>?, ?, ?</sup>,

$$k_{n,ij} = \frac{4}{3} E_{ij}^* \sqrt{R_{ij}^* \delta_{n,ij}} \quad (5.7a)$$

$$k_{t,ij} = 8G_{ij}^* \sqrt{R_{ij}^* \delta_{t,ij}} \quad (5.7b)$$

with  $G_{ij}^*$  as the pair bulk modulus,

$$\frac{1}{G_{ij}^*} = \frac{2(2 + \nu_i)}{E_i} + \frac{2(2 + \nu_j)}{E_j} \quad (5.8)$$

The damping coefficients,  $\gamma$ , arise to account for the energy dissipated from the collision of two particles.<sup>?, ?, ?</sup> Whether the damping coefficient is local or global and the exact form of the coefficient is more important for loosely confined granular systems and dictates the way the system approaches an equilibrium state.<sup>?</sup> For the case of our tightly packed pebble beds, it suffices to use the efficient form of,<sup>?, ?, ?, ?, ?</sup>

$$\gamma_n = \sqrt{5\beta_{\text{diss}} m^* k_{n,ij}} \quad (5.9a)$$

$$\gamma_t = \sqrt{\frac{10}{3}\beta_{\text{damp}} k_{t,ij} m^*} \quad (5.9b)$$

with  $\beta_{\text{damp}}$  as the damping ratio, and the pair mass,  $\frac{1}{m^*} = \frac{1}{m_i} + \frac{1}{m_j}$ . For a stable system with  $\beta_{\text{damp}} < 1$ , the damping ratio is related to the coefficient of restitution,  $e$ ,

$$\beta_{\text{diss}} = -\frac{\ln e}{\sqrt{\ln^2 e + \pi^2}} \quad (5.10)$$

### 5.2.4 Time integration

Having expressed the contact mechanics of the discrete element method, we now need a means of integrating the kinematics of the particles. The most common means of marching in time with DEM is the velocity-Verlet algorithm.<sup>7</sup> In this algorithm we integrate Eqs. 5.1 with half-steps in velocity, full steps in position, and then finally the complete step in velocity (the two half-steps in velocity are often compressed into a single, full step, as we will do below). Here we will explicitly show the integration for the translational degrees of freedom.

The force field defined by Eq. 5.1a is rewritten in terms of the acceleration of the particle. For clarity in expression, the per-particle subscripts ( $i$ ,  $j$ , etc.) will be temporarily omitted. Instead, time-varying quantities will have a subscript to refer to their temporal location. Quantities measured or evaluated at the current timestep will have subscript  $t$  (note this does not refer to tangential directions!). Eq. 5.1a is rewritten as

$$\mathbf{a}_t = \mathbf{g} + \frac{\mathbf{f}_t}{m} \quad (5.11)$$

The first step in the velocity-Verlet algorithm is to integrate the position of the particle by a full timestep based on the current timestep's velocity and acceleration. Note that the initial condition of the particle must specify both position and velocity for this step to be evaluated at the start, from then on the velocity is explicitly updated.

$$\mathbf{r}_{t+\Delta t} = \mathbf{r}_t + \mathbf{v}_t \Delta t + \frac{1}{2} \mathbf{a}_t \Delta t^2 \quad (5.12)$$

The particles at new positions interact as a function of their overlaps (see Eqs. 5.4). Acceleration at the full timestep is then calculated from the updated forces (of Eq. 5.11). In the last computational step, the velocity at the full timestep is found from an average acceleration,

$$\mathbf{v}_{t+\Delta t} = \mathbf{v}_t + \frac{\mathbf{a}_t + \mathbf{a}_{t+\Delta t}}{2} \Delta t \quad (5.13)$$

The velocity-Verlet algorithm is an efficient means of explicitly integrating the kinematic equations for all the particles in the ensemble but, as an explicit method, the size of the timestep must be carefully chosen to avoid instabilities in the system. Stable, critical timesteps and means of circumventing unreasonably small timesteps will be addressed in § 5.4. Additionally, we have contended with the Lagrangian tracking of the particles momentum but we have still to deal with energy transfer through the packed beds which is just as important for our packed beds of ceramic breeder material. The heat transfer will be tackled in § 5.3.

### 5.3 Granular heat transfer

In an analogous way we handled the momentum of every particle in DEM with Newton's laws of motion, the Lagrangian tracking of energy of each particle is obtained via the first law of thermodynamics. We treat each particle as a single distinct object and thus do not consider any internal temperature gradients (a point which we alluded to in § 4.3). The temperature of particle  $i$  is governed by

$$\rho_i V_i C_i \frac{dT_i}{dt} = Q_{s,i} + Q_i \quad (5.14)$$

where  $\rho$ ,  $V$ , and  $C$  are the density, volume, and the specific heat of the solid, respectively. Heat generation inside the particle is input with  $Q_s$  and the total heat transferred to/from particle  $i$  via conduction to all,  $Z$ , neighboring particles,

$$Q_i = \sum_{j=1}^Z Q_{ij} \quad (5.15)$$

The conductive heat transfer to neighboring particles comes from the inter-particle conduction formulas we derived in § 4.1, given in Eq. 4.2 with conductance of Eq. 4.5. They are repeated here for reference,

$$Q_{ij} = H_c(T_i - T_j)$$

and

$$H_c = 2k^* \left[ \frac{3F_{n,ij}R^*}{4E^*} \right]^{1/3}$$

### 5.3.1 Thermal expansion

The stresses predicted to act upon the solid breeder volume during operation of the fusion reactor arise from the differential rate of thermal expansion from the highly heated ceramic volume and the relatively cool structural container. Moreover, thermal creep motion is observed in pebble beds<sup>?, ?, ?, ?</sup> and is behavior we must capture in our model. Both of those phenomena can be traced to the thermal expansion of individual particles in the ensemble. Therefore, we introduce a thermal expansion formula that updates the diameter of each particle after a chosen amount of timesteps,

$$d_i = d_{0,i} [1 + \beta_i (T_i - T_{\text{ref}})] \quad (5.16)$$

where  $\beta_i$  is the thermal expansion coefficient (in units of 1/K),  $T_i$  is the temperature of the pebble at the current step, and  $d_{0,i}$  is the diameter of the pebble at temperature  $T_{\text{ref}}$ .

## 5.4 Stability study

As mentioned when the integration algorithm was introduced in § 5.2, the velocity-Verlet algorithm is a computationally efficient, second-order accurate means of updating the kinematics of all the particles in the ensemble.<sup>?</sup> The timestep of the integration, however, must often be very small to ensure that it is less than the time taken for a pressure wave to propagate through the particle. The timestep is further constrained by the quasistatic assumption used to derive the Hertzian contact force such that inertial and relaxation effects may be neglected.<sup>?</sup> We will also show that, in order to avoid heat energy to propagate further than a single pebble during a single timestep, the thermal timestep requirement is orders of magnitude larger than the mechanical timestep equivalent. And that the overall

minimum timestep is thus driven by the mechanical stability.

In tandem with the requirement on very small timestep, the thermal time-constants in the ceramic breeder zones can be many hundreds of seconds. These two conditions seem to conspire to force an unacceptably large requirement on the number of timesteps for a thermal DEM simulation and thus make numerical experiments impractical.

In this section we will analyze the calculation of a critical timestep based on the speed of a Rayleigh wave propagating along the surface of a particle. Then, with that knowledge in hand, we will argue for scaling certain physical properties to allow for faster simulations without sacrificing fidelity to the real physics of the problem.

#### 5.4.1 Critical dynamic timestep

If we wish to choose a timestep sufficiently small such that a pressure wave originating from the contact of one particle does not propagate to other neighboring particles during the timestep, we must choose a timestep smaller than the critical timestep defined by Rayleigh wave traveling through the solid.

When a force is applied to the surface of an elastic body, the force propagates along the surface at the wave speed first solved by John William Strutt, 3rd Baron Rayleigh<sup>7</sup> (when he wasn't discovering the scattering phenomenon explaining why the sky is blue or winning the Nobel prize for discovering Argon),

$$u_{\text{Ra}} = K \sqrt{\frac{G}{\rho}} \quad (5.17)$$

where, again,  $G$  is the shear modulus and  $\rho$  is the density of the elastic material. The  $K$  coefficient is a complicated function coming from Rayleigh's solution but can be approximated as<sup>7</sup>

$$K = 0.1631\nu + 0.876605 \quad (5.18)$$

which is valid for realistic values of Poisson's ratio,  $\nu$ , of elastic materials. From the inverse of the Rayleigh wave frequency, we can directly find a timestep for Rayleigh waves on a sphere of radius,  $R$ ,

$$\delta t_{\text{Ra}} = \frac{\pi R}{u_{\text{Ra}}} \quad (5.19)$$

When we write this for any particle,  $i$  in the ensemble (exchanging the shear for elastic modulus),

$$(\delta t_{\text{Ra}})_i = \frac{\pi R_i}{0.1631\nu_i + 0.876605} \sqrt{\frac{2(1 + \nu_i)\rho_i}{E_i}} \quad (5.20)$$

We allow for the particles in the system to have varying density, elastic modulus, and size. Therefore the critical timestep for the entire system is governed by the minimum value of any particle's Rayleigh timestep.

$$\delta t_c = \min_{\forall i} [(\delta t_{\text{Ra}})_i] \quad (5.21)$$

The ceramic materials identified for breeders have relatively high Young's moduli, on the order of  $10^{10}$  Pa. The smallest radius will be on the order of  $10^{-4}$  m. The ceramic density is approximately on the scale of  $10^4$  kg/m<sup>3</sup>. These values lead to a necessary timestep of

$$\delta t_c \propto 10^{-7}\text{s} \quad (5.22)$$

For a simulation that may last several hundreds of seconds of real time, this then requires more than  $10^9$  timesteps. If we have  $10^4$  particles in the simulation, each having their position integrated over a billion times, it becomes obvious that computational time is a major issue for our simulations of nuclear heating of ceramic breeder pebbles. If we are able to reduce the critical timestep (while perhaps decreasing the simulation time), the simulations will be much more practical for research use.

### 5.4.2 Critical thermal timestep

In § 4.1, we introduced the dynamics of heat transfer between contacting particles in an ensemble. As we integrate the energy of an individual particle in time, we must also ensure that energy would not propagate through a particle faster than a single timestep can capture. In analogy to the critical timestep for mechanical stability (e.g. Eq. 5.19), we write for particle  $i$ ,

$$\delta t_{\text{Bi}} = \frac{\rho_i C_i V_i}{H_c} \quad (5.23)$$

where  $\rho_i C_i V_i$  represents the inertial resistance to changing the temperature of  $T_i$  and the conductance,  $H_c$  represents the speed at which energy is delivered to  $T_i$  from contact conduction. Then from the definition of  $H_c$  we have given for smooth elastic spheres, this is also written as

$$\delta t_{\text{Bi}} = \frac{(4/3)\pi R_i^2 \rho_i C_i}{2k^*} \frac{R_i}{a} \quad (5.24)$$

For the material properties of lithium ceramics, as discussed for mechanical stability, we can expect

$$\frac{(4/3)\pi R_i^2 \rho_i C_i}{2k^*} \approx \frac{(10^{-4})^2 10^4 10^3}{10^0} = 10^{-1}$$

But from the requirements on Hertz theory in § 2.1, we have required that  $\frac{a}{R_i} \ll 1$ . Thus the timestep for stability in the energy calculation is utterly negligible compared to the mechanical stability.

Vargas and McCarthy<sup>7</sup> make similar arguments, giving the criteria as,

$$\frac{dT_i}{T_i - T_j} \ll 1 \quad (5.25)$$

and too note that the timestep requirement for thermal calculations are orders of magnitude less restrictive than the analogous restriction of the particle dynamics.

Thus we can be confident that any timestep chosen for dynamic stability in the DEM simulation will automatically satisfy the timestep for thermal stability.

#### 5.4.3 Simulation acceleration with scaled material properties

We rewrite Eq. 5.20 to facilitate a discussion on the parameters. Isolating each material term (neglecting the Poisson ratio) gives,

$$\delta t_c \propto R_i \times \rho_i^{1/2} \times E_i^{-1/2} \quad (5.26)$$

## 5.5 Pebble failure modeling

The discrete element method has been used for studies in a variety of fields for studying inter-particle forces and the homogeneously distributed force networks that arise in packed beds (for example, see Ref.<sup>?</sup>). The discrete element method was also used in the fusion community to attempt to model failure initiation and propagation.<sup>?, ?, ?</sup> They too observed that a relatively few number of high-force networks, distributed throughout the bed supported the external mechanical loads. The even distribution of the force networks was used to defend the development of a probability-based predictor for failure. We make use of the probability argument of Zhao, et al. for the current study.<sup>?</sup> Their basic premise is that probability distributions of strength curves for pebble crushing have been observed (see, for example crush loads of Ref.<sup>?</sup>). Then in DEM models, a probability distribution of inter-particle forces are also observed. Overlaying the two probabilities resulted in seemingly random locations of pebbles satisfying the failure criteria – not strictly along the high-force chains running through packed beds.

We apply the theory of Zhao, et al. in the following manner. If pebbles fail at random locations, we may de-couple the task of predicting pebble failure ( i.e. finding the mechanical or thermal load that causes a pebble to fail) from the task of modeling the ramifications of pebble failure. In our model, we begin with a starting point of a packed bed and then simply

flag pebbles at random for ‘failing’. For our first model of failure, after a pebble has been flagged it is removed from the system entirely. The removal disrupts the meta-static state of the ensemble and the remaining pebbles re-settle. In reality, the ceramic pebbles generally break into just a few large pieces that remain in the system. Under development is a method for recreating that behavior in the DEM domain, it will be reported in future studies.

## 5.6 DEM solver

### 5.6.1 Numerical Implementation Overview

The primary computational tools used in this study is LAMMPS (Large-scale Atomic/Molecular Massively Parallel Simulator);<sup>7</sup> a classical molecular dynamics code. The package of code, maintained by Sandia National Labs (<http://lammps.sandia.gov>), has many features making it particularly attractive for our use on the simulation of pebble beds. LAMMPS is open-source and written in highly-portable C++ allowing customization of any feature used in modeling. LAMMPS runs with distributed-memory message-passing parallelism (MPI) and provides simple control (manual or automatic) of the spatial-decomposition of simulation domains for parallelizing. Perhaps most importantly, LAMMPS provides an efficient method for detecting and calculating pair-wise interaction forces; the largest consumer of run-time in the DEM algorithm.<sup>7</sup> We build the code as a library so that LAMMPS can be coupled to other numerical tools; we use the scripting language of Python (Python 2.7) as an umbrella code to call LAMMPS routines with the full availability of Python libraries.

LAMMPS by default provides a rudimentary method of modeling of granular particles (the term ‘granular’ here differentiates the ‘discrete element’ of molecules or atoms from larger-scale granular particles of powders or pebbles); LAMMPS has been used for studying granular material since at least 2001 when Silbert, et al.<sup>7</sup> studied granular flow on inclined planes. However, the usefulness of LAMMPS for studying granular systems was greatly enhanced by LIGGGHTS (LAMMPS Improved for General Granular and Granular Heat Transfer Simulations), a suite of modules included on top of LAMMPS. LIGGGHTS has

many academic and industrial contributors from around the world, with the code maintained as open-source by DCS Computing, GmbH.

Briefly, some notable features the LIGGGHTS code brings to the LAMMPS environment include: Hertz/Hooke pair styles with shear history, mesh import for handling wall geometry, moving meshes, stress analysis of imported meshes, a macroscopic cohesion model, a heat transfer model, and improved dynamic load balancing of particles on processors.<sup>?</sup> Both LIGGGHTS and LAMMPS are distributed under the open-source codes under terms of the Gnu General Public License.

We will review some of the important physical models used in LAMMPS/LIGGGHTS as they relate to the important features we wish to investigate for packed beds of pebbles in fusion reactors.

### 5.6.2 other solver info

Time-discretization of the integration of Eq. 5.1 is handled by the core Large-scale Atomic/Molecular Massively Parallel Simulator (LAMMPS) code released by Sandia National Laboratories.<sup>?</sup> The code calculates velocity and position via the semi-explicit velocity-Verlet integration. The algorithm is stable with a global error of approximately  $O(\Delta t^2)$  for displacement; details can be found in Ref.<sup>?</sup>

In the process of the study, to demonstrate the ability of the dynamic integration to capture resettling (and any possibly asymmetries), some beds were generated wherein the failure of pebbles was slightly localized near one or both  $x$ -walls. The profile of the pebbles near the top of the stack, after resettling, are shown in Fig. 8.3.

In our work, we occasionally required a fully quiesced bed. To determine when this occurred, the total kinetic energy of the entire ensemble was monitored and a packed bed was considered to have completely settled once the kinetic energy of the system was less than  $10^{-9}$ ; similar to the process described in Ref.<sup>?</sup>

The granular heat transfer equations are layered onto the LAMMPS code via a package

of code named LIGGGHTS (LAMMPS Improved for General Granular and Granular Heat Transfer Simulations<sup>7</sup>). Parallelization of the code is straightforward with LAMMPS and we run the code on 128 nodes of UCLA’s Hoffman2 cluster for typical run times of 18 to 24 hours per routine (e.g. filling, packing, heating, etc.).

# CHAPTER 6

## Modeling coupled computational fluid dynamics and discrete element method (CFD-DEM)

[talk about how lacking the DEM result is without the inclusion of helium in analysis. There are some Fusion papers on conductivity in vacuum and with helium]

We now consider the influence of helium on thermal transport of deposited nuclear energy as it is carried away by the cooled structural walls. We begin by considering the fluid in a continuum sense and the pebbles in a discrete one. The interactions of the fluid and solid are characterized by effective relationships in each discretized cell of fluid. We then consider an mesoscopic approach to the fluid-solid interaction with the Lattice-Boltzmann method.

The chapter begins with introduction of the coupled fluid dynamics - discrete element method (CFD-DEM) approach: governing equations, discretization techniques, and algorithms.

We then do LBM. And stuff.

### 6.1 Numerical Methodology

Models based on the discrete element method (DEM) are currently the only tools available that can extract information on individual pebble interactions. The DEM formulation provides information such as inter-particle forces and individual particle temperatures, which are necessary for predicting and simulating morphological changes in the bed (e.g. pebble cracking, sintering, etc.) However DEM alone is not able to capture the effects, neither on momentum nor energy, of an interstitial fluid. Therefore we present two fluid modeling

techniques to supplement the DEM computations. We will first discuss the fully dynamic coupling of the DEM model with a volume-averaged thermofluid model of helium. Then we will introduce the integration of our DEM packing structure into lattice-Boltzmann simulations of the entire bed-fluid system.

### 6.1.1 DEM

The discrete element framework introduced in § 5.2 is augmented with a drag force term to capture interaction with surrounding fluid velocity fields. To accomplish this, we simply include a drag force to the Newtonian balance of forces given in Eq. 5.1. The momentum balance now reads:

$$m_i \frac{d^2 \mathbf{r}_i}{dt^2} = m_i \mathbf{g} + \mathbf{f}_i + \beta_i V_i \Delta u_{if} \quad (6.1)$$

where  $\Delta u_{if} = u_f - u_i$ , is the relative velocity between the fluid and pebble,  $i$ , and the inter-phase momentum exchange coefficient,  $\beta_i$ , acts upon the pebble volume (not to be confused with the damping coefficient introduced in § 5.2). Similarly, the energy equation now includes

$$m_i C_i \frac{d^2 T_i}{dt^2} = Q_{n,i} + \sum_{j=1}^Z Q_{ij} + \beta_{E,I} A_i \Delta T_{if} \quad (6.2)$$

where  $\Delta T_{if} = T_f - T_i$ , is the relative temperature between the fluid and pebble,  $i$ , and the inter-phase energy exchange coefficient,  $\beta_{E,i}$ , acts upon the pebble surface area,  $A_i$ .

The trajectory of pebble  $i$  is updated based on the force terms on the right hand side of Eq. 6.1: gravity, contact forces between particles (or particle-wall), and a drag force. Similarly, the temperature of the particle updates with the terms from Eq. 6.2: nuclear heating rate, inter-particle conduction, and now a heat transfer with surrounding fluid.

Drag forces from fluid flows through packed beds are found from volume-averaged, empirical correlations of either numerical or experimental studies. Considering a small region

of a packed bed surrounding our particle of interest,  $i$ , the nondimensional drag force is found only as a function of the local packing fraction of that region. In the zero Reynolds number limit, the nondimensional drag force reduces to a Stokes flow correlation that is only a function of the local packing fraction value,  $\phi$ . For the value of particle Reynolds numbers seen by the helium purge gas, this is the dominant term. However, for a complete discussion of the nondimensional drag terms see Refs. 5, 6. The correlation used in this study comes from the results of numerical studies of packed beds by Koch and Hill.<sup>7,8,9</sup> To arrive at their relationships, they did many lattice-Boltzmann simulations of porous flow.

$$\beta_i = \frac{18\nu_f\rho_f}{d_i^2}(1 - \phi)F \quad (6.3)$$

where

$$F = \epsilon(F_0 + \frac{1}{2}F_3\text{Re}_{p,i}) \quad (6.4)$$

Stokes flow

$$F_0 = \begin{cases} \frac{1+3\sqrt{\phi/2}+(135/64)\phi\ln(\phi)+17.14\phi}{1+0.681\phi-8.48\phi^2+8.16\phi^3} & \text{if } \phi < 0.4 \\ 10\frac{\phi}{(1-\phi)^3} & \phi > 0.4 \end{cases} \quad (6.5)$$

and high Reynolds contribution

$$F_3 = 0.0673 + 0.212\phi + \frac{0.0232}{(1 - \phi)^5} \quad (6.6)$$

The packing fraction and void fraction in any fluid cell is calculated by summing through all the volumes of  $k$  particles located in that cell (or the complement thereof)

$$\phi = \sum_{i=1}^k \frac{V_{p,i}}{\Delta V_f} \quad (6.7)$$

Other forces, such as Magnus forces, are inconsequential on predominantly stationary packed beds and are not considered.

The inter-phase energy transfer coefficient is of the same form as a traditional heat transfer coefficient and is calculated from the Nusselt number for the helium flow (with conductivity  $k_f$ ) through a packed bed.

$$\beta_{E,i} = \frac{\text{Nu}_i k_f}{d_i} \quad (6.8)$$

Li and Mason<sup>7</sup> summarize correlations for Nusselt number as a function of Reynolds number for packed beds with the following equations

$$\text{Nu} = \begin{cases} 2 + 0.6(1 - \phi)^n \text{Re}_p^{1/2} \text{Pr}^{1/3} & \text{Re}_p < 200 \\ 2 + 0.5(1 - \phi)^n \text{Re}_p^{1/2} \text{Pr}^{1/3} + 0.2(1 - \phi)^n \text{Re}_p^{4/5} \text{Pr}^{1/3} & 200 < \text{Re}_p \leq 1500 \\ 2 + 0.000045(1 - \phi)^n \text{Re}_p^{9/5} & \text{Re}_p > 1500 \end{cases}$$

where  $n = 3.5$  was found to fit best for small particles in dilute flows. [we should find a new value for high packing fraction]

Thus we have a formulation whereby a known fluid flow field and temperature throughout the domain, we can calculate the influence of that fluid on every particle's position and temperature. Next we will cover how we can calculate the flow field based on a volume-averaged influence of particles on the fluid.

### 6.1.2 Volume-averaged CFD Helium

The technique of coupling CFD to DEM was first proposed by Tsuji, et al<sup>9</sup>. In this formulation of the helium flow, a fluid cell is much larger than the individual particles (in application, this meant approx. 5-6 particles per cell) and as such, the particles themselves are not resolved in the fluid space but are simply introduced via volume-averaged terms. Therefore momentum and energy of a fluid flow through a solid phase is governed by volume-averaged Navier-Stokes and energy equations<sup>10</sup>. These equations are applied to a discretized volume

of fluid space. For fluid cell,  $k$ , these are<sup>5</sup>:

$$\frac{\partial \epsilon_k \rho_f}{\partial t} + \nabla \cdot (\epsilon_k u_f \rho_f) = 0 \quad (6.9a)$$

$$\frac{\partial \epsilon_k u_f}{\partial t} + \nabla \cdot (\epsilon_k u_f u_f) = -\frac{\epsilon_k}{\rho_f} \nabla P_f + \nabla \cdot (\nu_f \epsilon_k \nabla u_f) - \frac{S_k}{\rho_f} \quad (6.9b)$$

$$\frac{\partial \epsilon_k T_f}{\partial t} + \nabla \cdot (\epsilon_k u_f T_f) = \nabla (\epsilon_k \epsilon \nabla T_f) - \frac{E_k}{\rho_f C_f} \quad (6.9c)$$

where the fluid void fraction is the complement of the solid packing fraction,  $\epsilon = 1 - \phi$ . The momentum and energy exchanges with the solid phase are represented in the source terms. They are volume-weighted sums of the drag forces and energy exchanges, respectively, for all particles in the discretized fluid cell:

$$S_k = \frac{1}{V_k} \sum_{\forall i \in k} \beta_i V_i \Delta u_{if} \quad (6.10a)$$

$$E_k = \frac{1}{V_k} \sum_{\forall i \in k} \beta_{E,i} A_i \Delta T_{if} \quad (6.10b)$$

The inter-phase momentum and energy exchange coefficients act as the communicators between the particle information from the DEM solver and the fluid fields from CFD. Thus the motion and energy of the fluid field are intimately coupled with the particle positions and energy, but computational time is preserved by only considering volume-averaged values in the fluid domain. The cross-communication between fluid and solid is accomplished with a coupling routine that is explained in detail in Refs. 11, 12.

### 6.1.3 Modeling Setup and Procedure

The pebble bed has dimensions in the x-y directions of  $20d \times 15d$ , respectively. There are structural walls, providing cooling, at the x-limits and periodic walls in the y-limits. 10 000 pebbles were loaded into the system which went to a height of approximately  $24d$  after the bed was vibration packed. The pebble bed had a roof loaded at the upper limit of the

*z*-direction that was lowered by force-control up to 6 MPa. This bed is referred to as the ‘well-packed’ bed. This was meant to simulate a fresh, densely-packed bed that is under compressive load during fusion operation. As such, this would be when pebbles would be likely to crack during operation. Therefore, based on the well-packed bed, a second bed was generated by simulating crushed pebbles; crudely the extensive crushing is simulated by simply removing 10% of the pebbles at random from the ensemble and then allowing the bed to resettle, from the now-imbalanced gravity and inter-particle forces, to a new stable packing structure. This bed is then referred to as the ‘resettled’ bed for the rest of the analysis. The intent is to deduce changes in thermomechanical properties from an ideally packed bed to one where significant cracking has altered the ideal morphology of the bed.

## CHAPTER 7

### Modeling lattice-Boltzmann Method (LBM)

## **Part IV**

# **Cases studied**

# CHAPTER 8

## DEM studies

The discrete element method (DEM) is used by many ceramic breeder researchers to model the interaction of individual pebbles in an ensemble in an effort to obtain a more detailed understanding of pebble beds than is possible with experimental measurements of effective properties. For example see Refs.<sup>?, ?, ?, ?, ?, ?</sup>

### 8.1 DEM study: effective conductivity with disrupted packing

Our three-dimensional system consists of mono-dispersed particles of diameter  $d$ . The particles are constrained by two rigid walls in the  $x$ -direction at locations of  $x = \pm 10d$  and periodic boundary conditions in the  $y$ -direction located at  $y = \pm 7.5d$ . Gravity acts in the downward  $z$ -direction and the particles are bound from below by a rigid wall at  $z = 0$ . The size of the system allows approximately 10 000 particles to fill to a height of approximately  $z = 30d$ . The volume was chosen to represent the long, tall, narrow channels seen in many solid breeder module designs.<sup>?, ?, ?</sup>

#### 8.1.1 Material properties

For this study, the material was chosen as lithium metatinatate with all properties coming from Ref.<sup>?</sup> they are summarized in Table 8.1

Table 8.1: Maximum load and nominal tension.

E (GPa)	$\nu$	k (W/m-K)	C (J/kg-K)	$\alpha$ (1/K)
126	0.24	2.5	1156	$15 \times 10^{-6}$

### 8.1.2 Methodology

text

All the test cases begin with a common starting point of a filled, lightly packed volume of 10 550 pebbles. The pebbles are poured into the volume from above and come to rest under the influence of gravity (see Fig. 8.1). Initially, to recreate how we may pack solid breeders in reality, we attempted vibration simulations in order to pack the pebbles into a more dense state. However, we found the same packing states (from a void fraction standpoint) could be realized in a more computationally-simple manner by lowering a  $z$ -plane wall onto the top of the packed bed until it experienced some small force. This pour-press-packing routine was repeated many times and all the beds exhibited the same force on the top wall at roughly the same packing fraction. We took the last case, with a packing fraction (volume of  $N$  pebbles per total volume) of  $\phi_{bl} = 62.9\%$ , as our baseline configuration. The packed bed state was saved and used as a starting point for numerous ‘failed’ cases to be described later.

For the baseline case, we assigned an initial temperature of  $T_{ref}$  to both the pebbles and the  $x$  walls, then set a constant nuclear heating source on each pebble. The nuclear energy raised the temperature of the pebbles while the walls remained at  $T_{ref}$  for cooling. The process ran until a steady state was reached (for example, see Fig. 8.2); the total thermal energy of the bed,  $E = \sum_i^N m_i C_i T_i$ , was monitored and the simulation completed when the value was constant. At steady state, we analyzed thermomechanical characteristics of the pebble bed such as effective thermal conductivity, average coordination number, temperature profiles in the bed, and inter-particle contact forces.

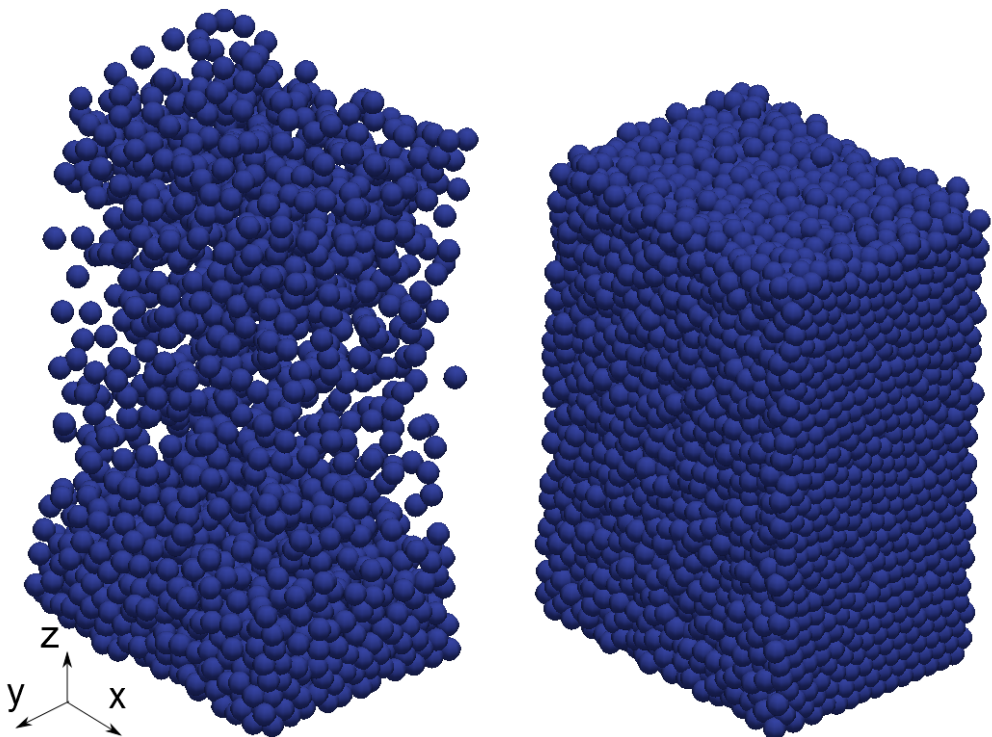


Figure 8.1: Demonstrating the pouring process of  $N = 10550$  pebbles into the control volume with an early (left) and late (right) snapshot.

As mentioned in Sec. 5.5, in this study we model pebble failure without considering the cause of failure. This is done by randomly selecting pebbles from the ensemble, regardless of forces acting upon the pebble, and removing them entirely. When a pebble is removed, the neighboring pebbles react due to the imbalance of forces and the bed settles into a new configuration. We differentiated the failed beds by their percentage of failed pebbles:  $\eta = \text{number of failed pebbles per original ensemble size}$ . After failing we again applied our heating routine.

### 8.1.3 Pebble Bed Heat Transfer: Test Case

In our pebble bed test case, we establish heat transfer that is essentially one-dimensional in the  $x$ -direction. The pebble bed has very little variation of forces and temperatures in the  $y$ -direction due to the periodic boundary condition at the edges of the domain. Gravity

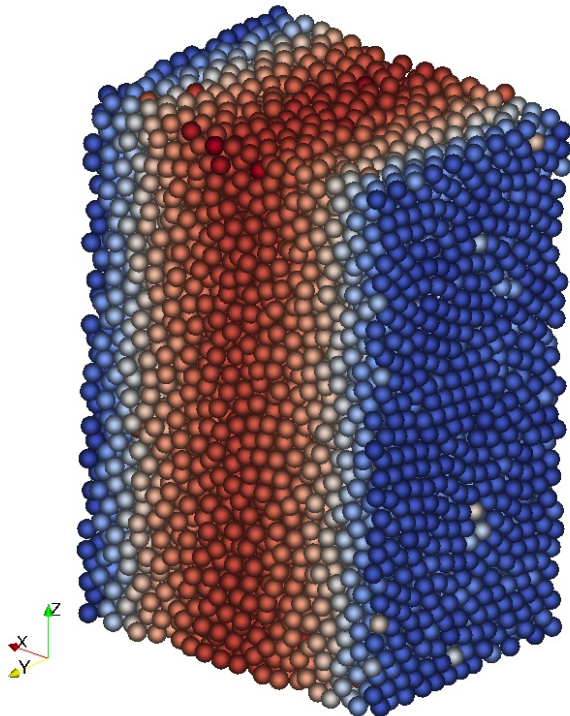


Figure 8.2: Temperature distribution of pebbles in the 10% failed bed. At the end of steady-state heating, a one-dimensional profile is evident in all pebble beds studied here. The pebbles are receiving nuclear heating. Cooling proceeds through the pebbles in contact with the walls in the  $x$ -direction. [color online]

effects are minor in the overall heat transfer and induce only a slight  $z$ -dependency to the results. With the one-dimensional assumption, we step back into a continuum mechanics formulation to aid us in finding an effective thermal conductivity of our numeric pebble bed.

A steady state for a material with constant temperature boundary conditions ( $T(\pm 10d) = T_s$ ) and nuclear heating has the following heat equation

$$0 = \frac{d^2T}{dx^2} + \frac{q'''}{k_{\text{eff}}} \quad (8.1)$$

In this continuum mechanics formulation, we are assuming that the nuclear source,  $q'''$  term is applied evenly over the entire volume. In our DEM formulation, our source term applies to a single pebble. To find the effective thermal conductivity of our pebble bed, we must reconcile this discrepancy. This is accomplished with the exchange of

$$q''' = \frac{Q_{\text{tot}}}{V_{\text{tot}}} = \frac{Q_s N}{300 H d^2} \quad (8.2)$$

where  $H$  is the average height of the top layer of pebbles. We apply symmetry about the centerline and impose our boundary conditions to solve the differential equation. If we take the temperature of the midplane as  $T(0) = T_0$ , we back-out an effective thermal conductivity (ETC) as

$$k_{\text{eff}} = \frac{Q_s N}{6H(T_0 - T_s)} \quad (8.3)$$

We will use this formulation to analyze and compare our test-case pebble beds.

The aim of this study was both to discover the impact of pebble failure on thermomechanical properties as well as determine the impact as a function of the number of failed pebbles. To satisfy the latter, we created beds with  $\eta = 1\%, 5\%, 10\%$ , and  $15\%$  of pebbles failed.

We first compare steady-state temperature profiles in the test beds against the one-dimensional theory of Eq.8.1. To find the temperature profile in  $x$ , we create volumes of

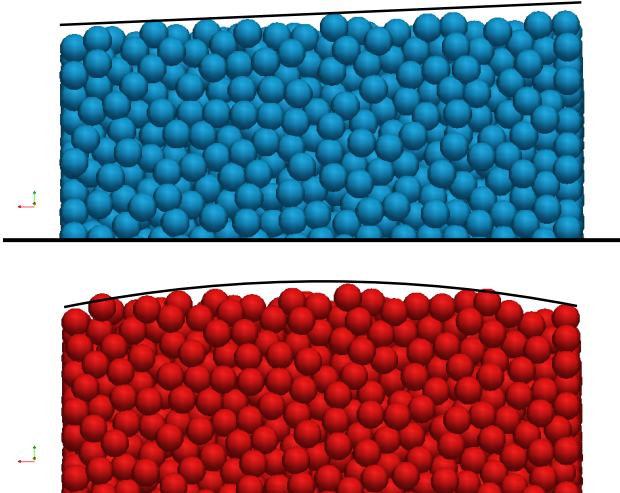


Figure 8.3: Demonstrating the dynamic resettling from an example study done on location bias to pebble failure. The top image had the pebbles near the left wall biased to fail. The bottom image had a bias for the pebbles near both walls to fail. The lines are drawn as an aid to the eye.

width  $\Delta x$  that extend through the limits of the  $y$ - and  $z$ -directions. We then find the  $n$  pebbles residing in the slices and take the mean value of their temperatures,  $\langle T \rangle = \sum_i^n T_i / n$  of all pebble temperatures that have coordinates inside the slice. Below we will omit the notation  $\langle T \rangle$  with the understanding that temperatures are volume-averages. Using the volume slices, we also find the average coordination number,  $\langle Z \rangle = \sum_i^n Z_i / n$ , normalized average contact force,  $\langle F^* \rangle = [\langle F \rangle / \langle F_{bl} \rangle_{\max}]^{1/3}$ , and the normalized average temperature difference between pebbles in the slice,  $\langle \Delta T_{ij} \rangle / (T_0 - T_s)_{\text{bl}}$ ; parameters which are discussed later.

When analytically solving Eq. 5.14, we introduce nondimensional temperature,  $\theta_{1D} = (T - T_s) / (T_0 - T_s)$ , and spatial,  $x^* = x / L$ , variables and the solution becomes purely geometric;  $\theta_{1D} = 1 - x^{*2}$ . We plot this theoretical solution against the temperature profiles coming from the steady-state DEM simulation in Fig. 8.4. We find that all our models had a nearly perfect match to a one-dimensional prediction, validating the calculation of effective thermal conductivity in this study.

Another concern we had for pebble failure, was the phenomenon of ‘jamming’ during resettling that would possibly leave pebbles isolated from their neighbors (apart from those they are resting upon). Such an isolated pebble would have no strong pathway for heat transfer and heat up much higher than that of its neighbors. Evidence of pebble isolation and ‘hot-spots’ would be apparent in Fig. 8.4 as localized deviations of data points from the quadratic profile. However, no deviations are seen in the data and we conclude that hot-spots will not be a concern in a packed bed.

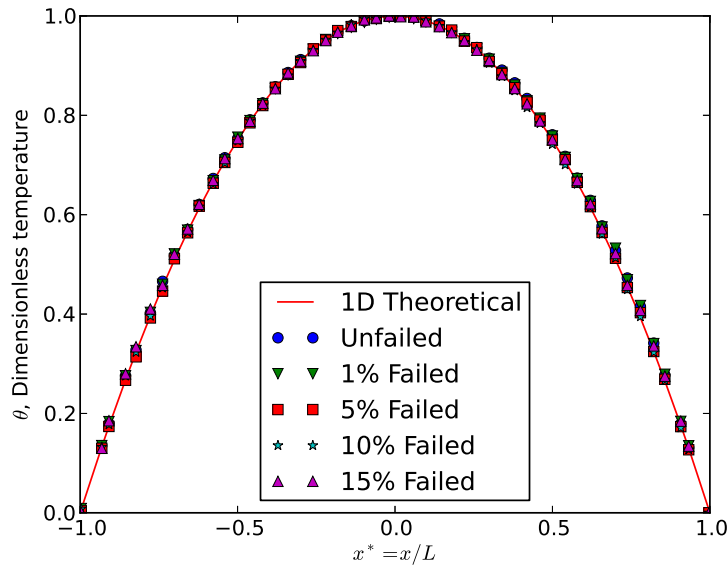


Figure 8.4: The nondimensional temperature profiles for each test case follow the theoretical shape of a one-dimensional, constant  $k$ , continuum solution.

The effective thermal conductivity is found for all of our pebble beds, via Eq. 8.3, then normalized against the conductivity of the baseline ensemble ( $k_{\text{eff}}^* = k_{\text{failed}}/k_{\text{bl}}$ ). Figure 8.5 shows the decreasing ETC with pebble failure. When 15% of the pebbles are crushed in a pebble bed, the ETC has fallen all the way to only  $k_{\text{eff}}^* = 0.30$ . This large reduction is especially important in light of the already poor thermal management of virgin pebble beds that, even in helium environments, have been experimentally measured at only approximately 1 W/m-K (see, e.g., Refs.<sup>?,?</sup>). In well-packed pebble beds, the ETC is generally related to the packing fraction. In Fig. 8.5, this relationship seems weak as the effective conductivity

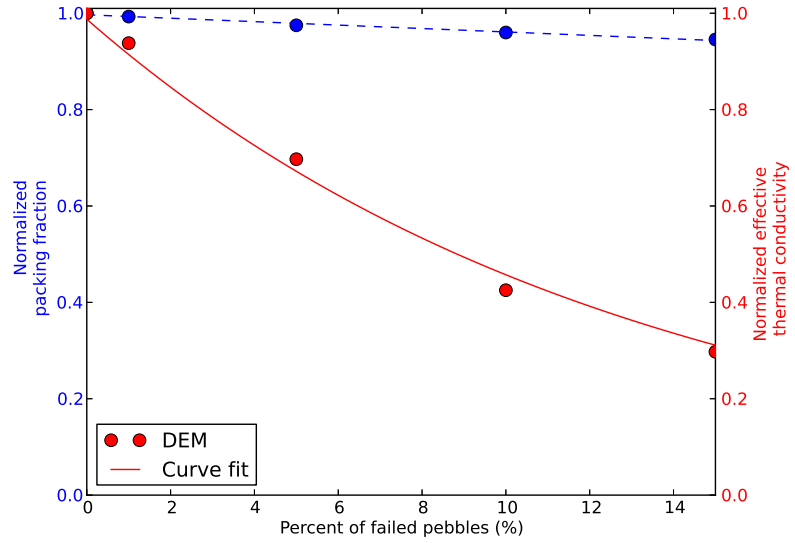


Figure 8.5: The normalized effective thermal conductivity (solid line) follows an exponential decay relationship with amount of failed pebbles. The normalized packing fraction (dashed line), compared to thermal conductivity, is relatively constant and is more closely fit to a linear reduction.

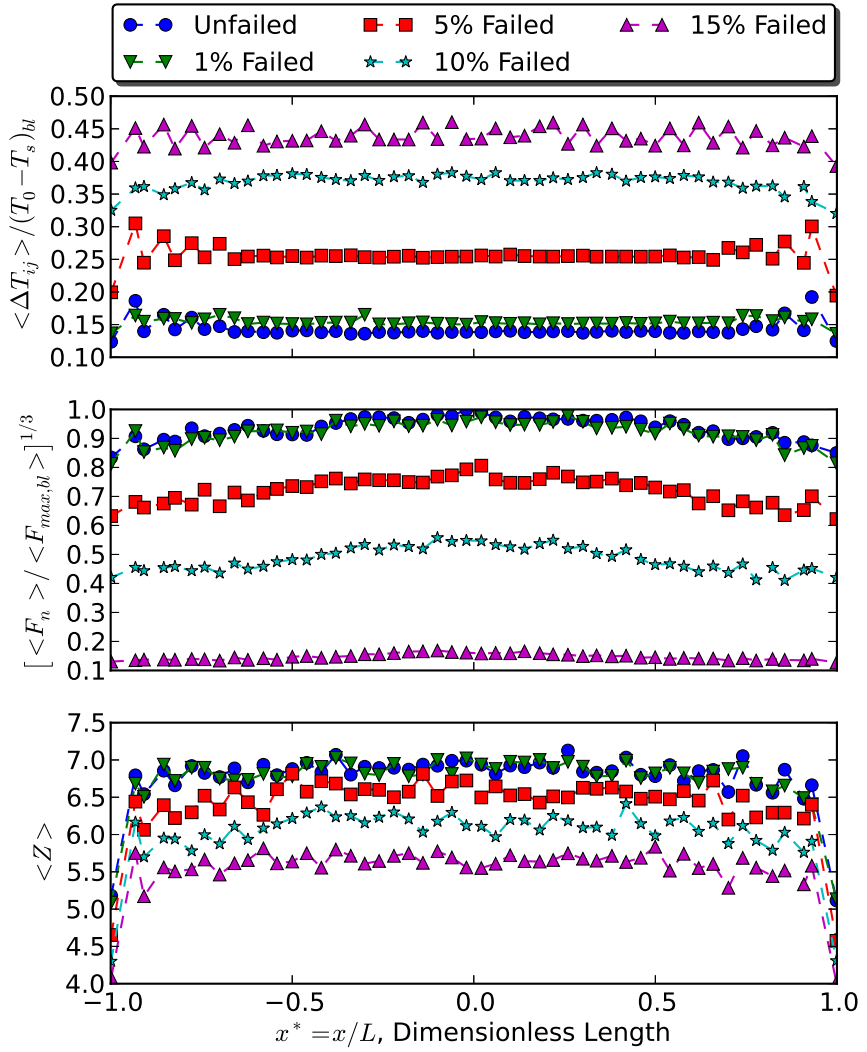


Figure 8.6: Average temperature differences between neighboring pebbles (top), contact forces (middle) and coordination numbers (bottom). The profiles of average coordination number and contact forces in the bed decrease in value with increasing pebble failure. Fewer and weaker contacts will reduce the possible paths of heat transfer from a pebble and this results in higher average temperatures between neighbors.

drops much more rapidly than does the packing fraction as the number of broken pebbles in the ensemble increases. To find the cause of decrease in conductivity and to make use of the information provided by DEM tools, we look to other parameters than the packing fraction.

From Eq. 5.14, in the steady-state, the energy input by nuclear heating must be balanced by the transport of heat out of a pebble into its neighbors. Inter-particle heat transfer is dictated by the number of neighboring contacts, temperature difference between pebbles, and the thermal conductance,  $h_{ij}$  through the contact area. The thermal conductance is, itself, a function of material properties (which are essentially constant here) and the force at the contact, going as  $h_{ij} \propto F_n^{1/3}$ . Thus, the net heat out is a function of the three variables as

$$Q_{\text{net}} = f(Z, F_n^{1/3}, \Delta T) \quad (8.4)$$

The variables affecting  $Q_{\text{net}}$  are plotted in Fig. 8.6. The average coordination number, shown in the bottom plot, decreases from a mid-line value of about 7.0 at the steady-state of the baseline case down to a mid-line value of 5.5 for the 15% failed bed; a reduction of about 80%. But this number doesn't compare with the large reduction in ETC which was  $k_{\text{eff}}^* = 0.30$ . Clearly, there are fewer contacts in the pebble bed after failure but this alone does not account for the reduction in ETC.

Much more dramatic, seen in the center plot, is the reduction in average normal force seen by pebbles after many of the neighbors fail and are removed from the system. From the baseline down to the 15% failed case, the contact forces are dramatically reduced to about  $\langle F^* \rangle = 0.1$ . This reduction in force is joined by an increase in average neighbor temperatures which are 3 times higher for the bed with most failed pebbles when compared to the baseline.

The results shown in Fig. 8.6 demonstrate that the heat transfer through a pebble bed is simultaneously a function of the coordination number and inter-particle contact forces – which are both reduced as pebbles in the bed fail – as well as the temperature difference between pebbles at steady state – which increases as pebbles in the ensemble fail. Interest-

ingly, when a pebble bed has lower overall inter-particle contact forces fewer particles would be expected to break. This would imply that pebble breakage is self-dampening; as pebbles begin to break the ensemble quickly relaxes and avoids future pebble failure. So while we induced failure up to  $\eta = 15\%$ , such large values may not occur in real beds.

Another feature of Fig. 8.6 worth noting is the increase in averaged normal contact forces near the center of the bed relative to the walls. In the assumptions used to develop this simulation, we had noted the lack of localized force concentrations in a bed under an external mechanical load. However, in these results, owing to the nuclear heating temperature profile and thermal expansion of each pebble, there is a bias toward higher forces in the center of the bed. This result highlights the need for a model to predict failure initiation in place of the assumption of random pebble failure.

## 8.2 Study of Young’s Modulus

The fundamental assumption in the DEM formulation is that each pebble acts perfectly elastically and thereby adheres to Hertz theory for contacting spheres. With Hertz theory, one finds contact forces as a simple function of: the virtual overlap between two objects, the Young’s modulus of the contacting material (and Poisson ratio), and radii of the two. In past studies, the Young’s modulus of the ceramic materials used in DEM simulations was taken from historical data, for instance lithium metatitanate from Ref.<sup>?</sup>

Based on observations of experimental data from single pebble crush data, in this study we propose a new method of obtaining the Young’s modulus for a batch of ceramic pebbles as the historical values from literature are not always appropriate. Details of the motivation and physics are in § 11.1.

### 8.2.1 Numerical experiments setup

We model our pebble beds undergoing a standard stress-controlled uni-axial compression up to 6 MPa. We will measure the macroscopic stress-strain for some parametrically varied

pebble beds and compare the curves. At the moment of maximum stress, we can investigate the differences in contact forces of those pebble beds.

Our pebble ensemble is composed of 0.5 mm diameter lithium orthosilicate pebbles. The pebble beds are initiated and packed in the same manner as § 8.1. There are two main bed groups. Set A: the first set of three beds (A.1-3) contain a single type of pebble with  $E = 90$  GPa. Set B: the second set of four beds (B.1-4) contain ten types of pebbles with their Young's modulus assigned in a discrete, random way to satisfy the distribution seen from experimental data. For the DEM study, we fit to lithium orthosilicate pebbles where the average stiffness was  $\bar{E} = 49$  GPa. The description of the two sets of pebble beds is visually represented in Fig. 8.7. The pebble bed geometry was also the same used in the study of Ref.;<sup>7</sup> two virtual walls in the x-direction located at  $x_{\text{lim}} = \pm 20R_p$ , periodic boundaries at the limits of  $y_{\text{lim}} = \pm 15R_p$ , and a total of 8000 pebbles packed into the volume to an approximate height of  $z_{\text{lim}} = 20R_p$ .

Among both sets, a parametric study was done on pebble radius and coefficient of friction. The radii of pebbles in beds A.1, A.2, B.1, and B.2 were constant at  $R_p = .25$  mm. The radii of pebbles in beds A.3, B.3, and B.4 followed a Gaussian distribution about  $\bar{R}_p = 0.25$  mm:  $\mu_d = R_p$  and  $\sigma_d = R_p$ . The coefficient of friction was set at  $\mu = 0.2$  for beds A.1, A.3, B.1, and B.3; the coefficient of friction was  $\mu = 0.3$  for beds A.2, B.2, and B.4.

### 8.2.2 Results

A constant-velocity, uniaxial compression was applied to the pebble beds. A single cycle up to 6 MPa was used on all the beds. The macroscopic measurements of stress-strain are shown for all the pebble beds in Fig. 8.8.

Naturally, the pebble beds with smaller Young's modulus (with circle markers) are more compliant to external loads. The result is true regardless of the coefficient of friction or distribution of pebble radius studied here. Group B moved to an average strain of about 2.6% at 6 MPa, by comparison the beds of Group A only had strained 1.9 % on average

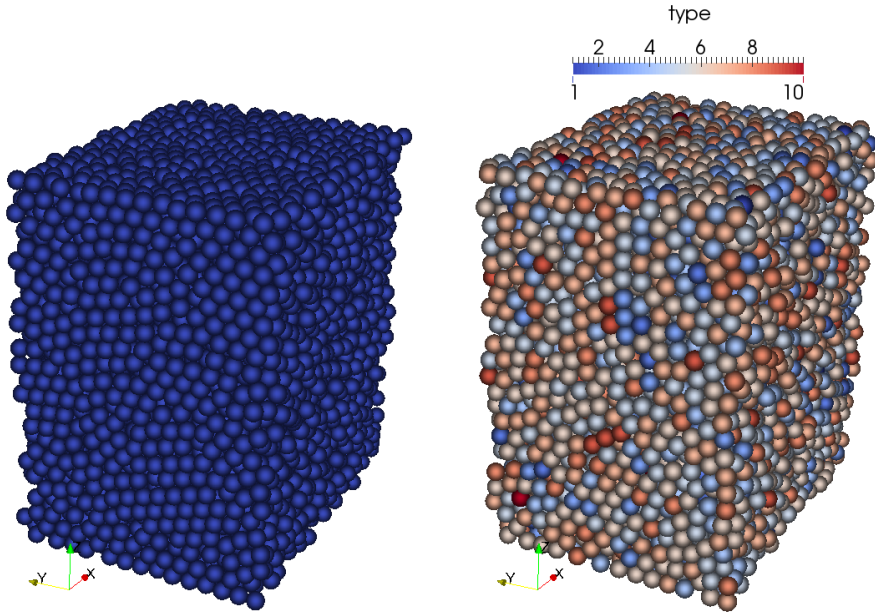


Figure 8.7: [color online] On the left, set A, a pebble bed with a single type, of  $E = 120$  GPa. On the right, set B, is a pebble bed with 10, randomly distributed types; each type corresponds to a reduced, apparent Young's modulus as derived from experimental data.

to reach the same stress. Among the beds of each group, pebble beds with constant radius pebbles behaved virtually the same as similar pebble beds with a Gaussian distribution on radius. An increase in the coefficient of friction had a moderate impact on the overall stress-strain response.

The parametric study here shows that the largest contributor to stress-strain response is the Young's modulus. The coefficient of friction and radius distribution had comparatively insignificant influence. A pebble bed geometry more directly comparable to oedometric compression experiments should be used to allow direct comparison and validation of the numerical models.

At the point of peak stress for each bed, we use DEM results to visualize the distribution of contact forces among all pebbles in the ensemble. A plot of the probability distributions of all the beds together, Fig. 8.9, shows that the majority of the contacts in all the beds are

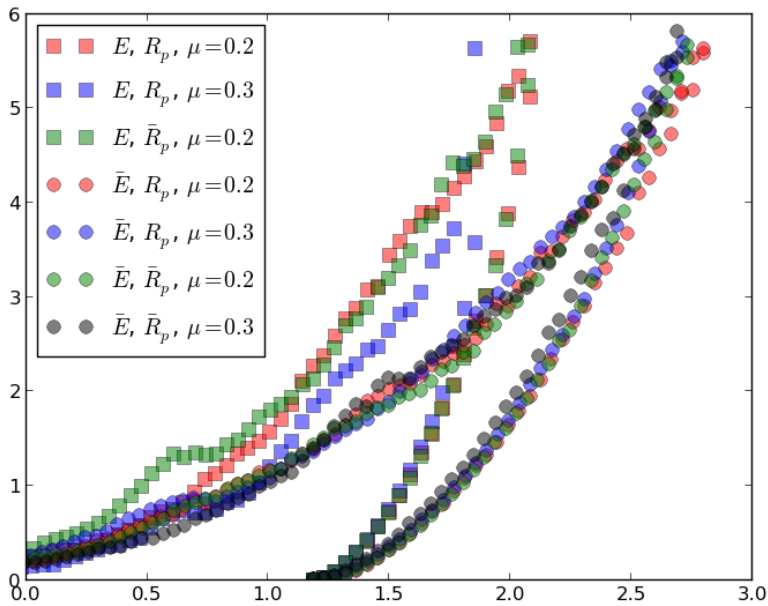


Figure 8.8: [color online] Stress-strain responses of pebble beds with: squares, constant Young's modulus; and circles, Gaussian distribution of Young's modulus. The constant Young's modulus beds all had much firmer responses for all parametric cases studied here.

equally small. There are a few overall trends we observe from the results however. The pebble beds with the constant Young's modulus are always higher for their comparable version with distributed Young's modulus. For pebble beds with comparable Young's moduli and radii, higher coefficients of friction generally have higher peak contact forces. Pebble beds' radius distributions have much less impact on peak contact forces than either coefficient of friction or Young's modulus. Another method of comparing overall contact force distributions is to consider predictions on pebble cracking which assigns a strength value at random to pebbles in the bed, according to Eq. 11.14. At the point of maximum stress, this is done and the results are shown in Tab. 8.2.

While overall the predicted number of broken pebbles is small, we compare similar parameteric pebble beds and in each case pebble beds with modified Young's modulus overall predict smaller percentages of broken pebbles. Pebble crushing is a major topic for the over-

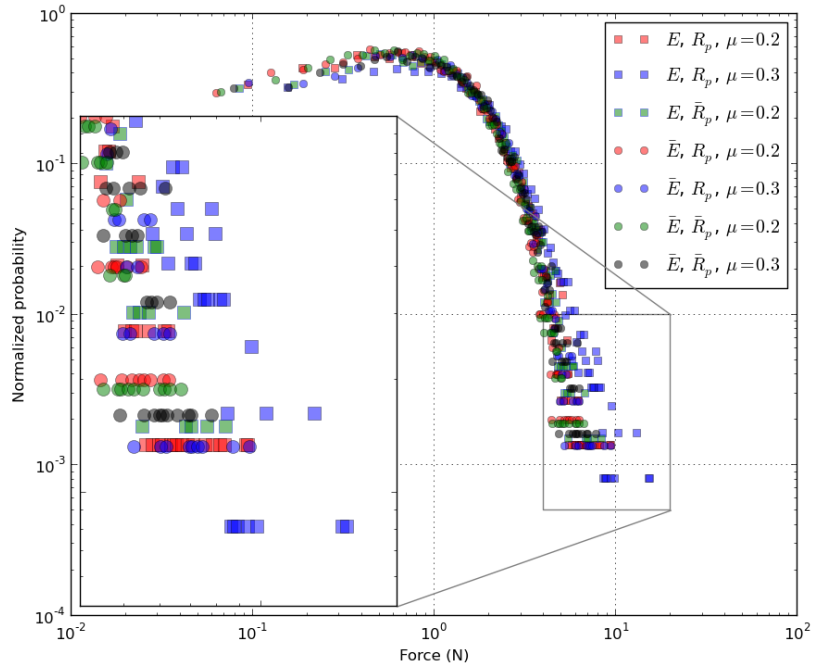


Figure 8.9: [color online] Probability distribution of contact forces in all the pebble beds studied here. Elastic moduli value is the largest contributor to higher peak contact forces among pebbles.

all evaluation of the feasibility of ceramic pebble beds in fusion reactors. This study reveals that past DEM work on pebble crushing was likely over-predicting the extent of crushing if the Young's modulus used in the study was much larger than the realistic response of individual pebbles.

### 8.2.3 Conclusions

Models based on the discrete element method have received considerable attention by ceramic breeder researchers. The method is attractive as it is based on material properties and forgoes many of the assumptions necessary in empirical equations of effective properties for continuum models. Variation in production techniques for ceramic pebbles lead to changes in ceramic microstructure, as evident in the wide distribution of crush loads reported in

Table 8.2: Comparisons for the two styles of Young's modulii used in the study.

Bed label	Parameters	Predicted crushed %
A.1	$E, R_p, \mu = 0.2$	0.3
A.2	$E, R_p, \mu = 0.3$	1.0
A.3	$E, \bar{R}_p, \mu = 0.2$	0.9
B.1	$\bar{E}, R_p, \mu = 0.2$	0.6
B.2	$\bar{E}, R_p, \mu = 0.3$	0.8
B.3	$\bar{E}, \bar{R}_p, \mu = 0.2$	0.4
B.4	$\bar{E}, \bar{R}_p, \mu = 0.3$	0.7

past studies, *e.g.* Refs.<sup>?,?</sup> By the same token, the different microstructures should naturally lead to variation in Young's modulus. However up to now values of Young's modulus used in numerical models are taken from values measured for large sintered pellets of ceramic materials. Based on single pebble experiments and the application of Hertz theory, a technique for introducing a modified Young's modulus into DEM models has been proposed here. DEM simulations show the impact of modified pebble elasticity on both macroscopic measurements of stress-strain curves as well as mesoscopic measures of inter-pebble contact force – with major implications for prediction of pebble crushing in ceramic pebble beds. The models applying the elasticity reduction factor,  $k$ , predict more compliant pebble beds and smaller peak contact forces in beds and thus fewer crushed pebbles.

### 8.3 Conclusions

The current study aimed at properly simulating a pebble bed with a specified fraction of the pebbles failing during operation; then determining the repercussions of the failures as they affect the macroscopic property of effective thermal conductivity. We used the assumption of

homogeneous, random locations of pebble failure to induce a failure routine without requiring external loads on the bed to permit beds that could be directly compared. After heating to a steady-state, an effective thermal conductivity was calculated for the pebble bed. The results show that small amounts of pebble failure correspond to large decreases in the conductive transport of energy through the pebble bed. The increase was due primarily to a drop in the inter-particle forces which lead to a large increase in temperature differences between neighboring pebbles. We note again, however, that this value has been calculated in the absence of interstitial gas so the results apply only to the reduction in energy transferred via inter-particle conduction.

The assumption of homogeneous distribution of pebble failure was found to be inappropriate after a pebble bed reached steady state nuclear heating. The scheme assumes no localization of average forces in the bed but we found an average force profile that had a maximum at the center and minimum at the walls. The next step of modeling will eliminate the error of such an assumption as we must combine failure prediction to failure outcome modeling.

# CHAPTER 9

## CFD-DEM studies

### 9.1 Pressure Drop

Before analyzing thermal results from the CFD-DEM coupling, the system was run at various particle Reynolds numbers and the overall pressure drop of the packed bed was measured. This value was compared against the well-known Kozeny-Carman and Ergun equations. The Kozeny-Carman is known to fit better with experimental data at very small Reynolds numbers. In Fig. 1 we see the CFD-DEM coupling model is providing bed-scale pressure drops that match very well with Kozeny-Carman over the Reynold's numbers applicable to helium purge flow in fusion reactors. The flow is visualized in Fig. 2. The pebble bed is clipped at the centerline to allow viewing of the helium streamlines. Apparent in the figure is temperature profiles in the helium from centerline to wall that qualitatively mirror temperature profiles in the pebble bed.

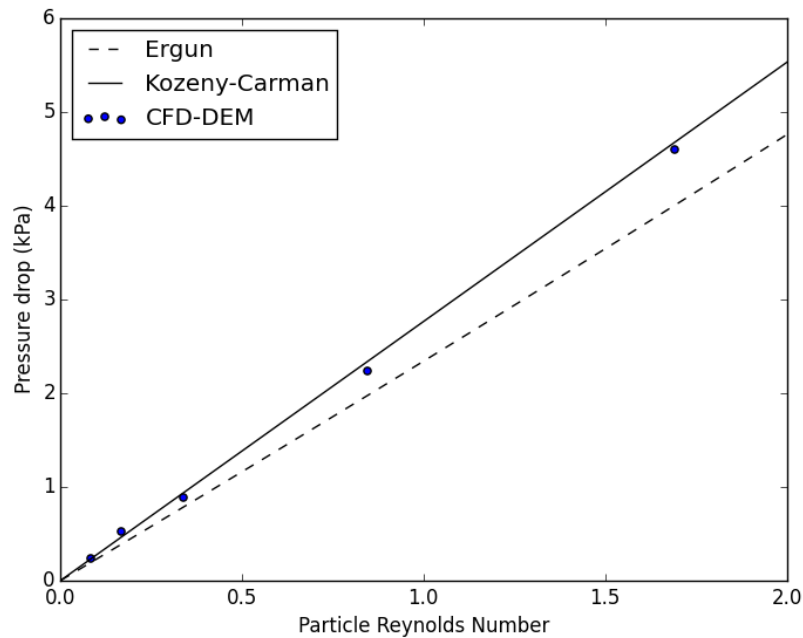
### 9.2 Effective thermal conductivity from CFD-DEM

#### 9.2.1 Stagnant interstitial fluid

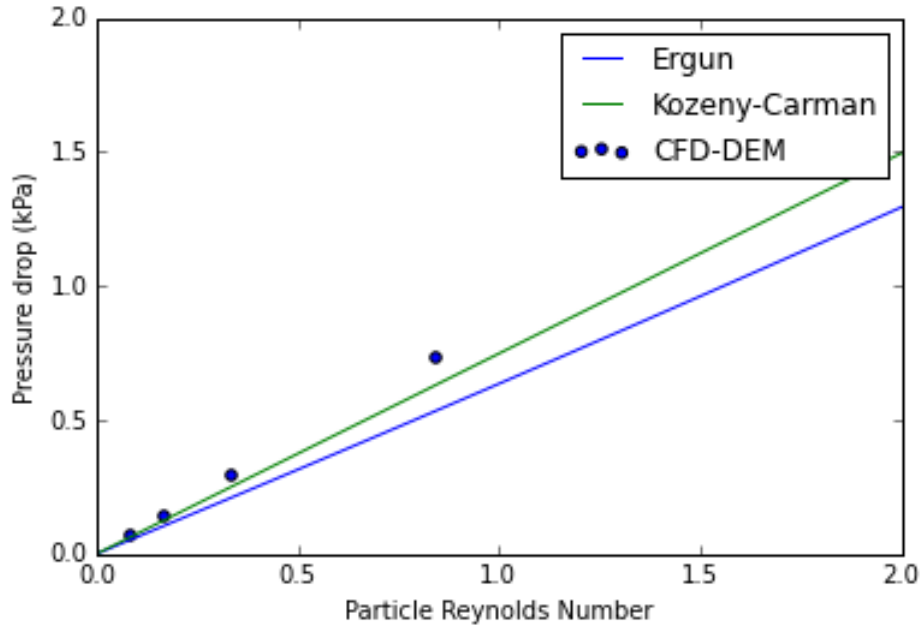
can use correlations for stagnant gas in packed bed.

#### 9.2.2 Purge gas

The well-packed and resettled pebble beds were run to thermal steady-state with nuclear heating and wall cooling in both pure DEM and coupled CFD-DEM simulations for com-



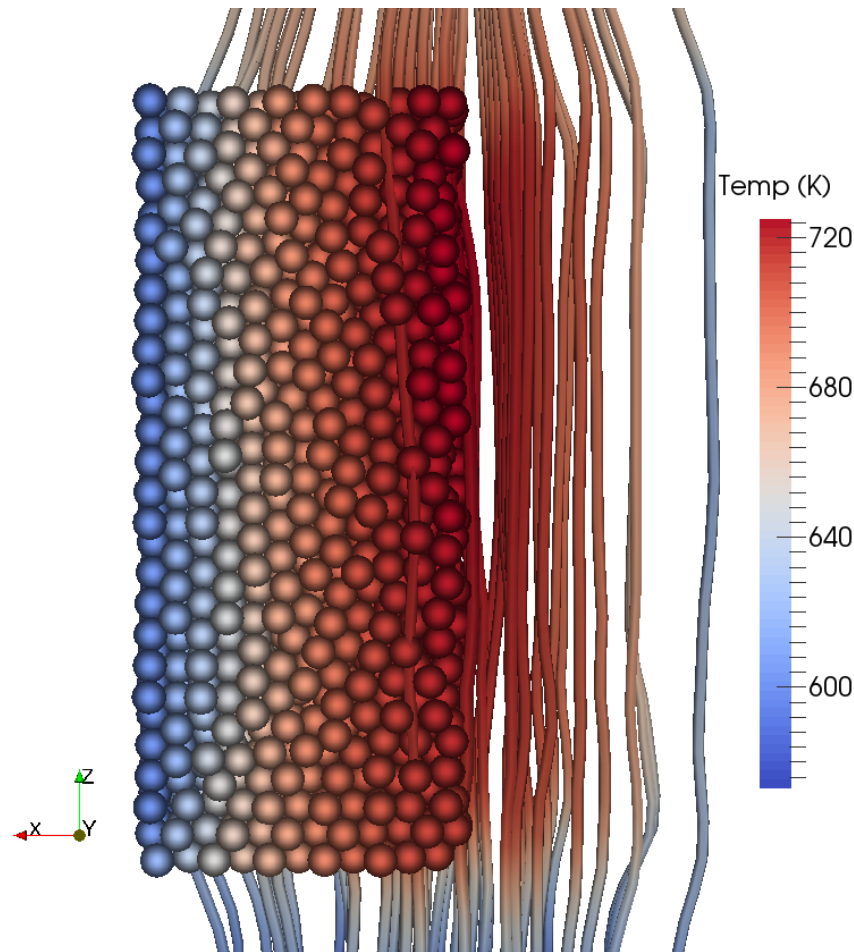
(a) Well-packed bed



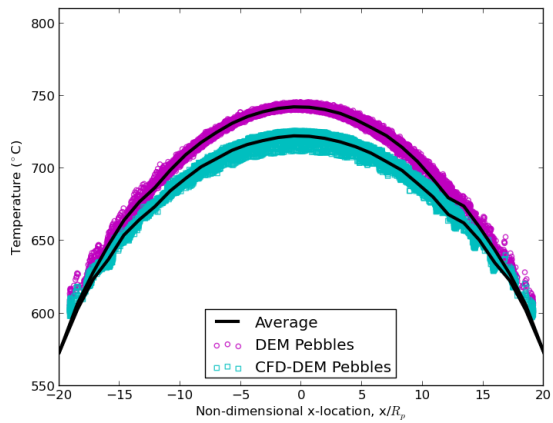
(b) Re-settled bed

Figure 9.1: Pressure drop calculations across packed beds, solved by CFD-DEM, fit well to the Kozeny-Carman empirical relation.

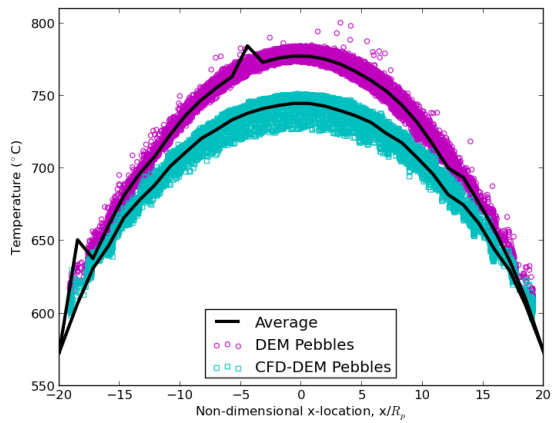
Figure 9.2: Cut-away view of the pebble bed with streamlines of helium moving in generally straight paths from inlet to exit.



parison. From steady-state temperature distributions, seen in the pebble scatter plots in Fig. 3, an average profile is calculated and an effective thermal conductivity computed. The values are tabulated in Table I. In the case of pure DEM, energy is transported solely along conduction routes in the ensemble. When the packing of the bed is disturbed, this results in a substantial drop in effective conductivity (a drop of 31%). The details of the conductivity reduction were studied extensively in Ref. 23. Perhaps more important than the reduction in effective conductivity, is the appearance of isolated pebbles. Because heat deposition is volumetrically applied, pebbles with poor conduction routes become much hotter than their neighbors. This is evident in the high temperatures seen in many of the pebbles in the right



(a) Well-packed bed



(b) Re-settled bed

Figure 9.3: Scatter temperature profiles of pebbles in a bed that is: well-packed (left) and resettled after 10% of pebbles were removed from crushing (right). The introduction of helium into the simulation contributes to both lower overall temperatures (higher effective conductivity) and the smoothing out of high temperatures of isolated pebbles.

figure of Fig. 3. Over-heating of isolated pebbles could induce sintering and impact their tritium release even when the average temperatures measured in the bed are well below sintering values. When CFD-DEM beds are analyzed, there is still a large reduction in effective conductivity (22% drop), but interesting to note is the lack of isolated pebbles with high temperatures. In the CFD-DEM scatter plot of the right image in Fig. 3, there is evidence of the reduced heat transfer in the same region as the isolated pebbles from the DEM bed, but the temperatures are much closer to the average values of neighboring pebbles. The helium purge gas has effectively smoothed out the temperatures and provided heat transport paths for any pebbles that have loose physical contact with neighbors. In spite of the 22% decrease in effective conductivity, the maximum temperature of the pebble bed only increased 6.2% (from 725 to 751 K) when helium is included in the model. This result is significant for solid breeder designers. They may choose a solid breeder volume such that in the event of extensive pebble cracking, the maximum temperature of the bed would remain within the ideal windows dictate for the lithium ceramics.

Table 9.1: Pebble bed values from the test matrix of the beds analyzed in this study.

	$k_{\text{eff}}$ (W/mK)		$T_{\max}$ (K)		$\frac{Q_h}{Q_{\text{nuc}}}$
	DEM	CFD-DEM	DEM	CFD-DEM	CFD-DEM
Well-packed	0.96	1.09	745	725	1.15
Resettled	0.66	0.85	800	751	1.52

An accompanying result is the increased amount of energy carried out of the system by the helium purge gas. In Table I, the last column provides the ratio of energy carried out of the system to the nuclear energy deposited into the bed. The amount of energy carried out by the helium increased from 1.15% to 1.52% from ‘well-packed’ to ‘resettled’. The CFD-DEM formulation maintains calculations of pebble-pebble interactions while dynamically coupling to the helium flow. The model demonstrates the ability of helium gas to smooth out any hot spots predicted by pure-conduction DEM formulations. Further, the

lattice-Boltzmann simulation, while not fully coupled to DEM, revealed important features of helium flow in volumetrically heated pebble beds – mainly the smearing of temperature profiles along the paths of cooling.

## **CHAPTER 10**

### **LBM studies**

# CHAPTER 11

## Pebble Interaction Analysis: Experimental Relationships

Many experiments were carried out on individual ceramic pebbles. While there are some measures from experiments that are immediately useful for qualitative comparisons, such as the crush strength between different batches of ceramics, most values are not obviously connected to analysis of the pebbles nor the pebble bed assemblies they make up. In this section we will show had careful examination of single pebble experiments can lead to predictions of not only strength in ensembles but also modifications of the fundamental properties of the ceramic pebbles.

In section § 11.1, we use single pebble experiments to validate the use of Hertz theory for contacting ceramic pebbles, but also determine the proper Young's modulus to use for the ceramics. In section § 11.2 we use the theory we developed in section ?? along with experimental data to begin to make predictions for survivability of pebbles in ensembles.

### 11.1 Elasticity reduction factor

In the study of individual pebble crush force (see § 11.1), the force-travel response curves of ceramic materials consistently exhibit distributions in the stiffness of the pebbles. For example, see the results of different lithium ceramic pebbles in Fig. 11.7. For DEM studies, we claim that interaction between these pebbles is well-represented by the Hertzian normal force as derived in § 2. For the discussion, we rewrite Eq. 2.16 here,

$$F_{n,ij} = \frac{4}{3} E_{ij}^* \sqrt{R_{ij}^*} \delta_{n,ij}^{3/2} \quad (11.1)$$

where  $\delta$  is the overlap between contacting spheres and  $\frac{1}{E^*} = \frac{1-\nu_i^2}{E_i} + \frac{1-\nu_j^2}{E_j}$ ,  $\frac{1}{R^*} = \frac{1}{R_i} + \frac{1}{R_j}$ . The contact force is directly proportional to the pair Young's modulus,  $E^*$ . Thus an accurate value of pebble Young's modulus is critical for an accurate calculation of contact force. For brevity, we do not include many details on DEM, but refer the reader to the original paper by Cundall and Strack<sup>7</sup> upon which all modern models are based.

We now present Hertz equation as it applies to a pebble, diameter of  $d_p$ , being pressed between two flat anvils with measured travel of one anvil as  $s$ :

$$F_n = \frac{1}{3} E^* \sqrt{d_p s^3} \quad (11.2)$$

and  $\frac{1}{E^*} = \frac{1-\nu_p^2}{E_p} + \frac{1-\nu_a^2}{E_a}$ . Where the subscript  $p$  refers to pebbles and  $a$  the anvils.

From Eq. 11.2, we see that standard Hertz theory, where we use a single value for Young's modulus from literature, is not appropriate for pebbles studied in ceramic breeders. If single values of  $E_p$  and  $\nu_p$  are employed, then variation in pebble diameters can not alone explain the variation of curves of Fig. 11.7.

### 11.1.1 Elasticity reduction factor

We propose to explain the behavior of individual pebbles (as in Fig. 11.7) with an assumption that the production technique yields pebbles with slightly different internal structures. The differences in internal structure then cause the pebble to have a different apparent modulus of elasticity; which will vary from some strong limit value. The strong value is the elastic modulus of highly sintered pellets reported in literature for the material,  $E_{\text{bulk}}$ . Assuming this strong value is the upper limit, imperfections in the pebbles will lead only to a reduction in this value. To quantify the deviation from the bulk, we introduce a  $k$  factor, defined as the elasticity reduction factor:

$$k = \frac{E_{\text{peb}}}{E_{\text{bulk}}} \quad (11.3)$$

where  $k \in [0, 1]$ .

If each pebble has a unique  $k$  value, this would quantify the spread in elastic responses seen in the experiments. The value is found by assuming that the pebbles are, in fact, behaving in a Hertzian manner, allowing us to back-out its  $k$  value, or in other words the unique  $E^*$  of that pebble by finding a best fit to the experimental curves.

From room temperature, we take the sintered pebble value for these  $\text{Li}_4\text{SiO}_4$  pebbles to be  $E_{\text{bulk}} = 90 \text{ GPa}$  and  $E_{\text{bulk}} = 124 \text{ GPa}$  for  $\text{Li}_4\text{SiO}_4$  pebbles. Then we iterate over all values of  $k \in [0, 1]$  and compare the Hertzian response to that pebble's force-displacement curve.

The data of Fig. 11.7a is fit in the manner described and the pebbles are all plotted against Hertzian curves with their own unique modified Young's modulus in Fig. 11.1. The modified Hertzian curves with apparent Young's modulus fits well with most of the pebbles' curves. Similar data is obtained for the pebbles of Fig. 11.7b but the results are omitted for conciseness.

One of the benefits of using DEM simulations is the ability to predict pebble cracking in an ensemble based on knowledge of the interaction forces. If we are over-predicting the contact forces based on inaccurate material properties, we are going to be over-predicting the impact of pebble cracking as well. An accurate description of the material properties is an important feature for ceramic breeder designers.

We will apply the modified Young's modulus distributions to pebble beds and compare the results to pebble beds simulated with standard Young's modulus from literature.

We introduced Hertz theory in § 2, and now we apply it to experiments for analysis of ceramic pebbles. The derivation of Hertz force can be found on page ?? but is given again here for reference.

$$F = \frac{4}{3} E^* \sqrt{R^*} \delta^{3/2} \quad (11.4)$$

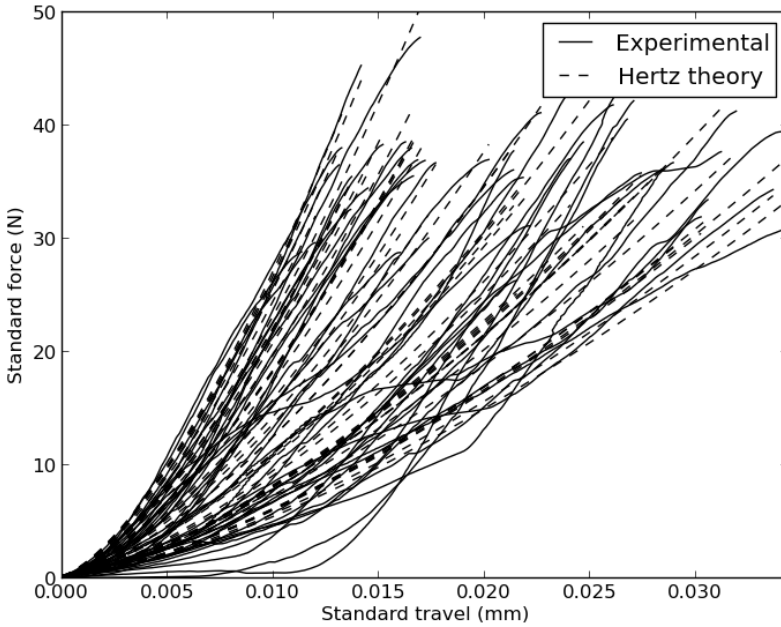


Figure 11.1: Experimental responses (solid) and fit curves of Hertzian equivalent with apparent Young's modulus (dashed).

and, again, the relative Young's modulus and radius are

$$\begin{aligned}\frac{1}{E^*} &= \frac{1 - \nu_i^2}{E_i} + \frac{1 - \nu_j^2}{E_j} \\ \frac{1}{R^*} &= \frac{1}{R_i} + \frac{1}{R_j}\end{aligned}$$

In experiments where we press a ceramic pebble between two platens, we measure the travel,  $s$ , rather than the pebble overlap, so we modify Eq. ?? to be represented in terms of travel ( $s = 2\delta$ ). Furthermore, for a pebble ( $R_i = R_p$ ) in contact with a smooth plane ( $R_j \rightarrow \infty$ ), the relative radius is simply  $R^* = R_p = d_p/2$ .

The Hertz force is now expressed as

$$F = \frac{1}{3} E^* \sqrt{d_p s^3} \quad (11.5)$$

Let's take a moment to discuss Eq. 11.5. The Young's modulus of the test stand platen

is a constant value. One might assume the Young's modulus of the ceramic is also a known, constant value. In that case, there should be only a single force response for every pebble of a given diameter. Using the material properties given in Ref.<sup>7</sup> for  $\text{Li}_2\text{TiO}_3$ , we plot a set of parametric curves based on diameter. The properties used for an nickel-alloy platen and  $\text{Li}_2\text{TiO}_3$  are given in Table 11.1. The curves are given in Fig. 11.2.

Table 11.1: Material properties used for  $\text{Li}_2\text{TiO}_3$  and nickel-alloy platen

$E_{\text{peb}}$	$\nu_{\text{peb}}$	$E_{\text{stand}}$	$\nu_{\text{stand}}$
(GPa)		(GPa)	
126	0.24	220	0.27

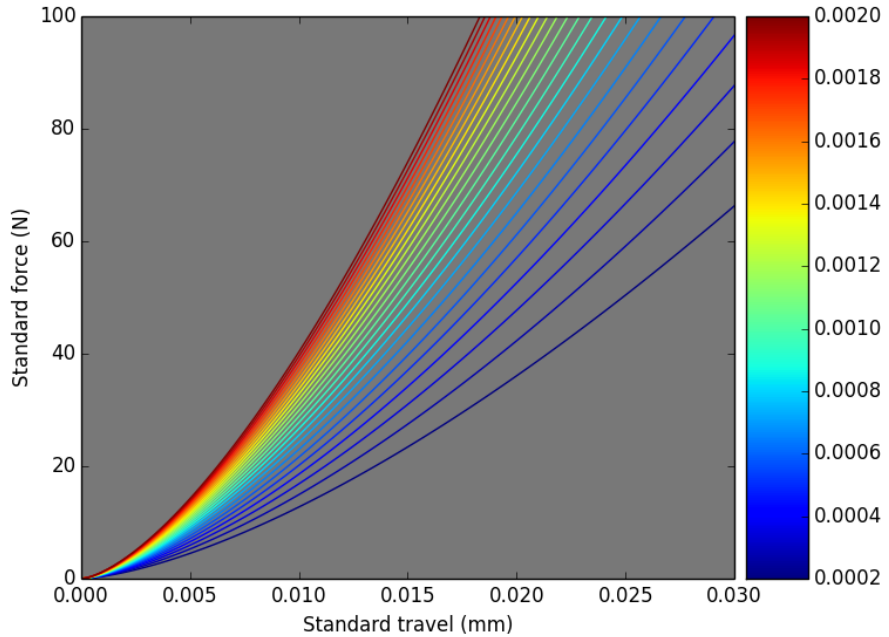


Figure 11.2: Hertzian responses of  $\text{Li}_2\text{TiO}_3$  pebbles compressed between platens. The colormap shows pebble diameters in m. The diameters span an order of magnitude from  $d_p = 0.2$  mm to  $d_p = 2$  mm.

Figure 11.2 clearly shows that if a pebble of a given diameter is strictly obeying Hertz

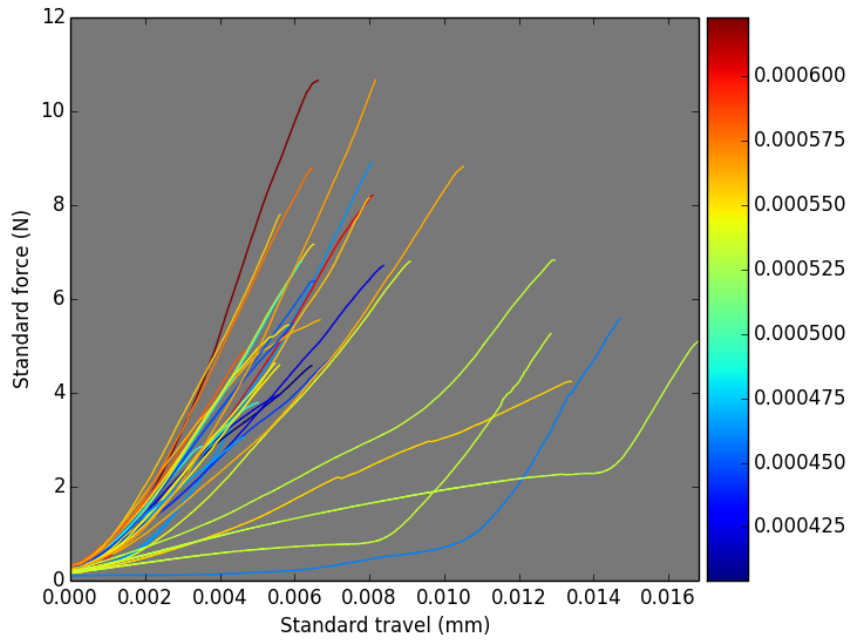
theory, there is only a single force-displacement curve it can follow. However, when experiments are performed on single pebbles we see quite different behavior for the F-s curves, see the curves of Fig. 11.3.

Figure 11.3a shows  $\text{Li}_4\text{SiO}_4$  pebbles as they are compressed between platens. Neglecting the handful of pebbles with very low force responses to high strain, there is a grouping of pebbles where there is a general trend that matches Fig. 11.2. The smaller diameter pebbles, in blue colors, have lower force responses for a given strain. Larger pebble diameters, in yellow-orange, are slightly higher overall in their force response. Finally, the largest diameter pebble in dark red has the highest force response for a given diameter. However, while the trends are *generally* similar to the theoretical Hertzian curves, there are noticeable spreads in responses. The responses of  $\text{Li}_2\text{TiO}_3$  pebbles of Fig. 11.3b, on the contrary, show almost no adherence to the expected diameter dependence of Hertz theory.

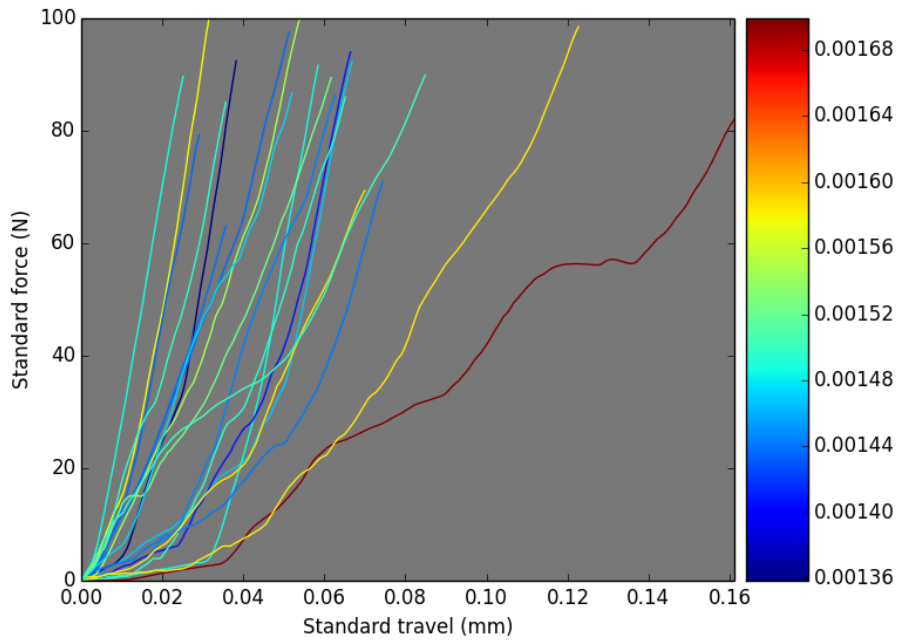
The behavior of pebbles observed in Fig. 11.3 lead us to conclude that variations in pebble diameter can not alone account for the variation in the F-s curves. The most reasonable source for a variation is in the Young's modulus of pebbles in a batch. Such a conclusion is important for implementation of Hertz theory in DEM algorithms.

We hypothesize that variation in the apparent Young's modulus of each pebble is rooted in the production of the pebbles which yields pebbles with slightly different internal structures. The differences in internal structure then cause the pebble to behave with different stiffnesses than the value expected from measurements of sintered pellets of lithium ceramics. In fact, we consider the sintered pellet Young's modulus,  $E_{\text{sp}}$ , as the upper limit for the pebbles and that most will emerge with values less than  $E_{\text{sp}}$ . To quantify the deviation of each pebble's  $E_{\text{peb}}$  from the sintered pellet, we introduce a  $k$  factor, defined as the elasticity reduction factor:

$$k = \frac{E_{\text{peb}}}{E_{\text{sp}}} \quad (11.6)$$



(a)  $\text{Li}_4\text{SiO}_4$  pebbles of approximately 0.5 mm diameter.



(b)  $\text{Li}_2\text{TiO}_3$  pebbles of approximately 1.5 mm diameter.

Figure 11.3: Force-displacement curves for two sets of experimental data, a batch of  $\text{Li}_4\text{SiO}_4$  pebbles and a batch of  $\text{Li}_2\text{TiO}_3$  pebbles. The colormap shows pebble diameters in m.

where

$$k \in [0, 1]$$

If each pebble has a unique  $k$  value, this would quantify the spread in elastic responses seen in the experiments. We find the value by assuming that the pebbles are, in fact, behaving in a Hertzian manner. This allows us to back-out a  $k$  value, or in other words the unique  $E_{\text{peb}}$  of that pebble by finding a best fit to the experimental curves.

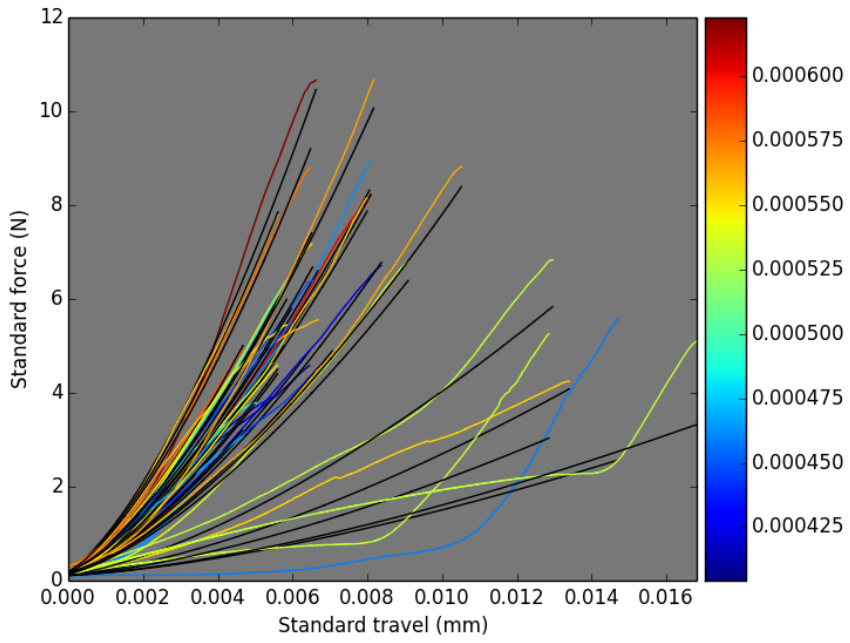
We take the sintered pebble value of Young's modulus for  $\text{Li}_4\text{SiO}_4$  to be  $E_{\text{sp}} = 90$  GPa and the value for  $\text{Li}_2\text{TiO}_3$  to be  $E_{\text{sp}} = 124$  GPa. Then we iterate over all values of  $k \in [0, 1]$  and compare the Hertzian response to that pebbles force-displacement curve. At each iteration, the L2-norm of the difference between Hertzian and experimental curves is used as the 'error'. The L2 norm,  $A$  for a given array,  $a$  is

$$\|A\|_F = \left[ \sum_{i,j} \text{abs}(a_{i,j})^2 \right]^{1/2} \quad (11.7)$$

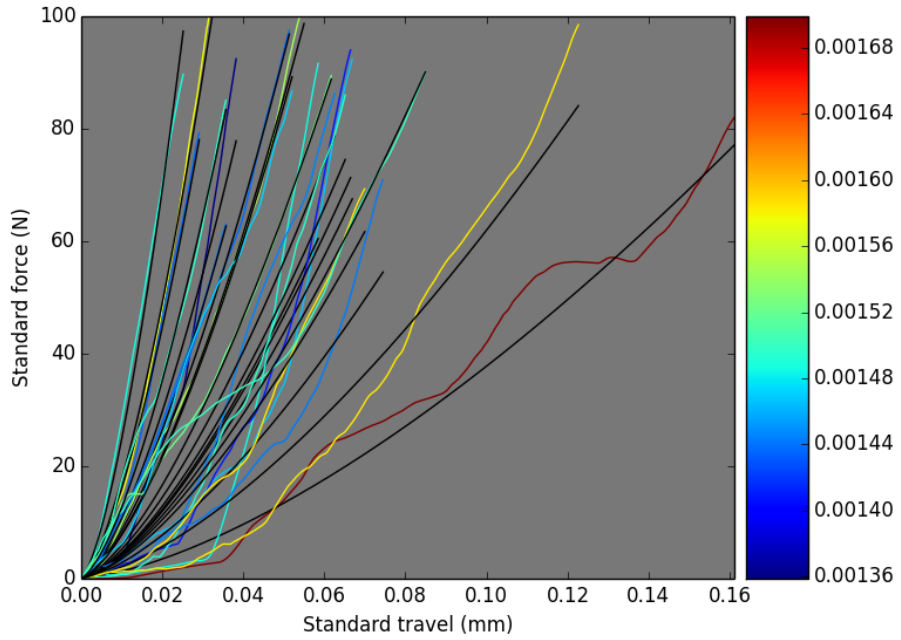
This is a convenient way to compare the error at every point along the force-displacement curves. When the error is minimized, the elasticity reduction value corresponding the minimum is recorded for that pebble. The Hertzian curves (in black) for each pebble are plotted in green against the experimental curves in Fig. 11.4.

Many of the curves in Fig. 11.4a seem to be fit well with a Hertzian curve with modified Young's modulus. The value of Young's modulus found for each pebble is plotted in Fig. 11.5. The Young's modulus of pebble numbers 0 to 4 are the very 'soft' pebbles seen with very low forces on Fig. 11.4a. The majority of pebbles behave with a Young's modulus between 30 and 70 GPa. On the upper end, a few pebbles acted very similar to their sintered pellet counterpart with approximate value of 90 GPa.

What remains is actually using these modified Young's modulus in DEM simulations to see if they more accurately reflect pebble bed macroscopic behavior. If so, it is assumed they will more accurately reflect the contact forces between pebbles in the ensemble.



(a)  $\text{Li}_4\text{SiO}_4$  pebbles of approximately 0.5 mm diameter.



(b)  $\text{Li}_2\text{TiO}_3$  pebbles of approximately 1.5 mm diameter.

Figure 11.4: Force-displacement curves for two sets of experimental data, a batch of  $\text{Li}_4\text{SiO}_4$  pebbles and a batch of  $\text{Li}_2\text{TiO}_3$  pebbles. The colormap shows pebble diameters in m.

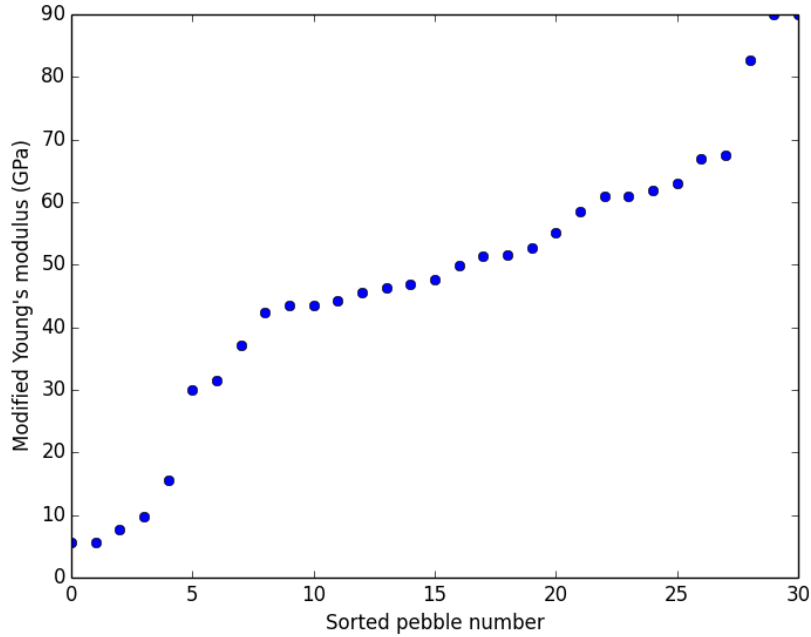


Figure 11.5: Distribution of modified Young's modulus for a batch of  $\text{Li}_4\text{SiO}_4$  pebbles. Most pebbles responded to compression with a Young's modulus well below the sintered pellet value of 90 GPa.

## 11.2 Strain energy measurements

### 11.3 Linking interactions with strain energy

Hertz theory is applicable to any two contacting elastic objects. In practice, we cannot probe the contacts of small particles and rely on experiments where we press pebbles between flat platens. Here we will develop a theory for connecting the results of the experiments with the interaction of two spherical objects.

To relate the situation in the lab to two particles, we first integrate the Hertzian force along the overlap to find the strain energy,  $W_\epsilon$ , of that contact.

$$W_\epsilon = \int_0^{\delta_c} F_n(\delta') d\delta' \quad (11.8)$$

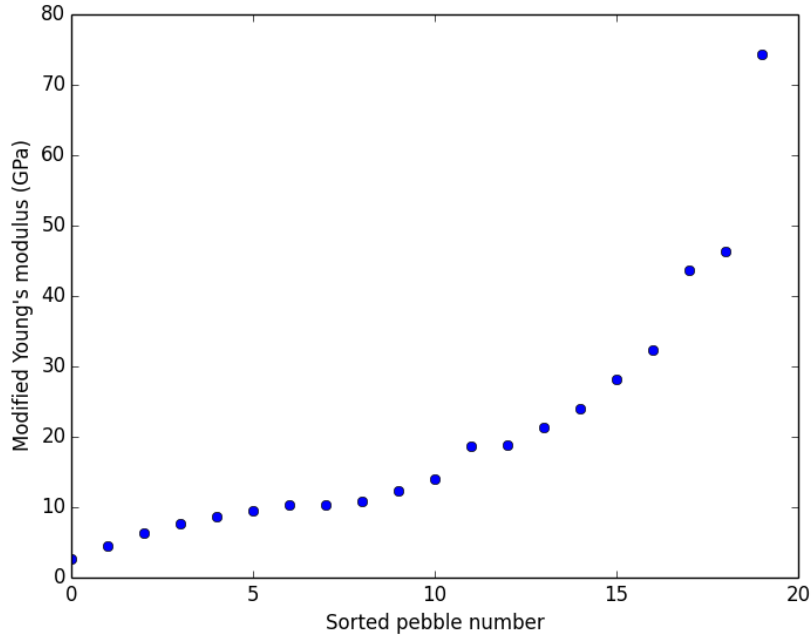


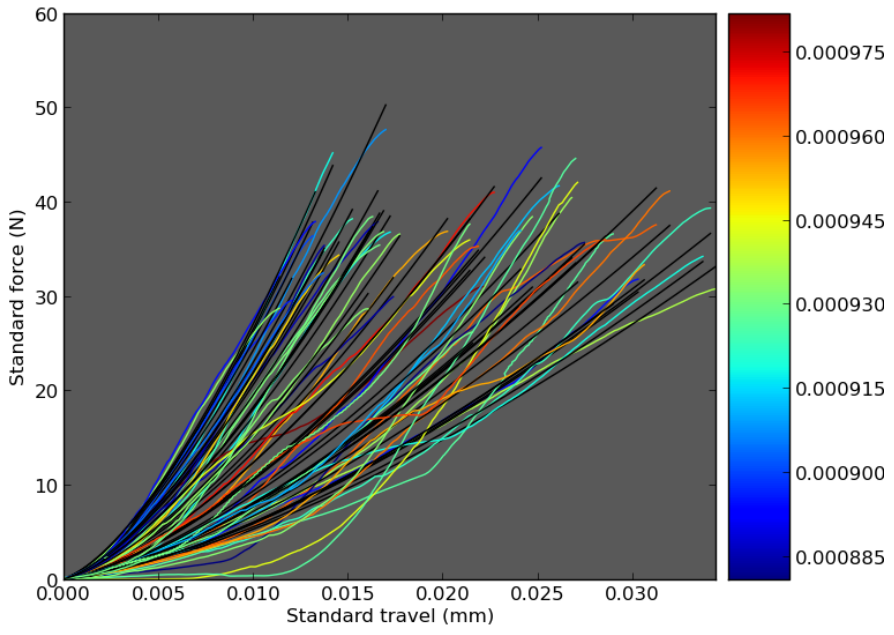
Figure 11.6: Distribution of modified Young's modulus for a batch of  $\text{Li}_2\text{TiO}_3$  pebbles. All pebbles responded to compression with a Young's modulus well below the sintered pellet value of 126 GPa.

where the upper limit of the integration is the critical overlap  $\delta_c$  (the meaning of this value will be explained in detail later). With the force defined from Eq. ??, this is straightforward to integrate.

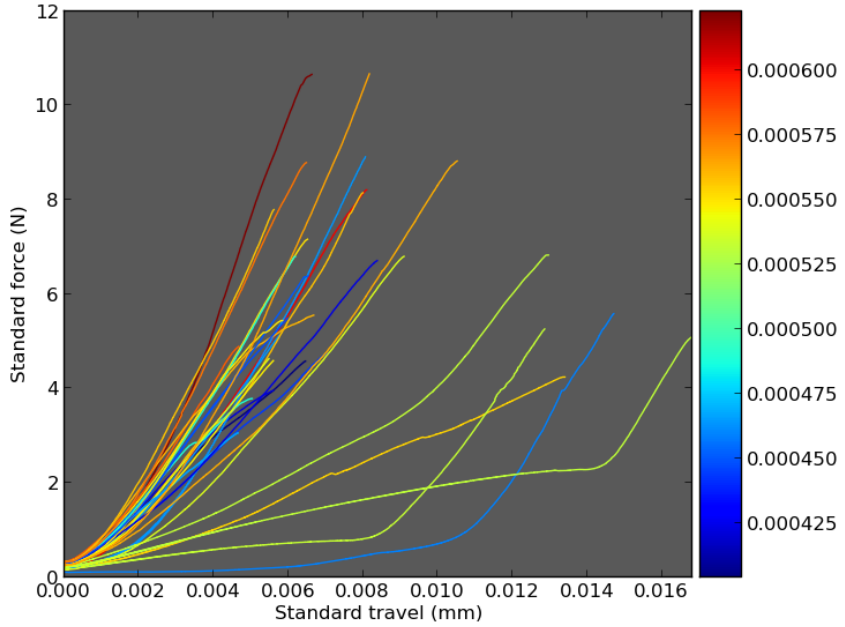
$$W_\epsilon = \int_0^{\delta_c} \frac{4}{3} E^* \sqrt{R^*} \delta'^{3/2} d\delta' \quad (11.9)$$

$$W_\epsilon = \frac{8}{15} E^* \sqrt{R^*} \delta_c^{5/2} \quad (11.10)$$

We will call the strain energy of the pebble compressed between platens as the lab strain energy,  $W_{\epsilon,L}$ . The strain energy of two particles in contact will be  $W_{\epsilon,B}$ . The assumption we make is that, if each interaction is integrated to the proper critical overlap, the strain energies will be equal at that point.



(a)  $\text{Li}_2\text{TiO}_3$  pebbles of  $d_p = 1 \text{ mm}$ .



(b)  $\text{Li}_4\text{SiO}_4$  pebbles of  $d_p = 0.5 \text{ mm}$ .

Figure 11.7: Force-travel responses of various lithiated ceramic pebbles of disparate diameters show similar behavior in distributions of responses. The colormaps differentiate the pebbles by diameter (in meters).

$$W_{\epsilon,L} = W_{\epsilon,B} = \frac{8}{15} E_B^* \sqrt{R_B^*} \delta_{c,B}^{5/2} \quad (11.11)$$

We solve for the interacting particle overlap as a function of the lab strain energy as

$$\delta_{c,B} = \left[ \frac{15W_{\epsilon,L}}{8E_B^* \sqrt{R_B^*}} \right]^{2/5} \quad (11.12)$$

This overlap can be reinserted to Eq. ?? to find the critical force of the interacting particles as a function of the critical strain energy of the lab. Doing this, we find:

$$F_{c,B} = C E_B^{*2/5} R_B^{*1/5} W_{\epsilon,L}^{3/5} \quad (11.13)$$

where  $C = \frac{4}{3} \left( \frac{15}{8} \right)^{3/5}$ .

In this analysis we have referred to a ‘lab’ and ‘particle’ for the two situations. In fact, the result is more general and can be used to relate any two scenarios. The only requirement is that both conditions adhere to the assumptions of Hertz theory. The ramifications of this relationship will be explored in more detail in ??.

### 11.3.1 Pebble crushing predictions

Along with proper material properties, we present a relationship to translate between the experimental data of crush force to a value that can be applied to DEM simulations. We relate crush force experimental data to predictions of crushing pebbles in an ensemble with:

$$F_{c,B} = \frac{4}{3} \left( \frac{15}{8} \right)^{2/5} (R_B^*)^{1/5} (W_{\epsilon,L})^{3/5} \quad (11.14)$$

where  $W_{\epsilon,L}$  is measured strain energy at the point of crushing from the experiment. This value follows a probability distribution and therefore imparts a distribution shape to the  $F_{c,B}$  prediction. At the peak load of 6 MPa we use the above prediction to determine how many pebbles would be cracking at this state of external pressure

## **Part V**

# **Future Work**

**Part VI**

# **Appendices**

## APPENDIX A

### Sphere with heat generation

We solve for the temperature distribution inside a single sphere of constant thermal conductivity with constant heat generation with a convective heat transfer boundary condition. To simplify to homogeneous boundary conditions, the temperature we solve for will be in reference to the fluid temperature,  $\mathbb{T} = T - T_f$ .

The energy equation in spherical coordinates with axial symmetry is,

$$\frac{1}{r} \frac{\partial^2}{\partial r^2} (r \mathbb{T}) + \frac{g}{k} = \frac{1}{\alpha} \frac{\partial \mathbb{T}}{\partial t} \quad (\text{A.1})$$

which is subject to the boundary conditions of a constant heat transfer coefficient at the surface,  $h$ ,

$$\left[ \frac{\partial \mathbb{T}}{\partial r} + \frac{h}{k} \mathbb{T} \right]_{r=b} = 0 \quad (\text{A.2})$$

and an axisymmetry at the center,

$$\left[ \frac{\partial \mathbb{T}}{\partial r} \right]_{r=0} = 0 \quad (\text{A.3})$$

The sphere will be at an isothermal initial temperature,

$$\mathbb{T}(r, 0) = \mathbb{T}_0 \quad (\text{A.4})$$

## A.1 Transformations

We first transform the system into the nondimensional forms as defined in § 4.3,

$$\begin{aligned}\theta &= \frac{T}{T_0} \\ \rho &= \frac{r}{b} \\ \tau &= \frac{t}{b^2/\alpha}\end{aligned}$$

The energy equation is then,

$$\frac{1}{\rho} \frac{\partial^2}{\partial \rho^2} (\rho \theta) + G = \frac{\partial \theta}{\partial \tau} \quad (\text{A.5})$$

$$\text{where } G = \frac{gb^2}{kT_0}$$

The next transformation will be to introduce  $U(\rho, \tau) = \rho \theta(\rho, \tau)$  as a transformation variable to simplify the differential equation of energy conservation. In the new variable formulation, the energy equation is,

$$\frac{\partial^2 U}{\partial \rho^2} + G\rho = \frac{\partial U}{\partial \tau} \quad (\text{A.6})$$

The boundary conditions are likewise transformed into,

$$\left[ \frac{\partial U}{\partial \rho} + (\text{Bi} - 1) U \right]_{\rho=1} = 0 \quad (\text{A.7})$$

and

$$U|_{\rho=0} = 0 \quad (\text{A.8})$$

with initial condition

$$U(\rho, 0) = U_0 = \theta_0 r^* = r^* \quad (\text{A.9})$$

## A.2 Solution

Because of the non-homogeneous form of the energy equation (due to the heat generation term), we will solve Eq. A.6 by breaking it up into two simpler problems,

1. A non-homogeneous, steady-state problem defined by  $U_{ss}(r)$
2. A homogeneous, time-dependent problem defined by  $U_h(r, t)$

The steady-state distribution  $U_{ss}$  is found from the solution of

$$\frac{\partial^2 U_{ss}}{\partial \rho^2} + G\rho = 0 \quad (\text{A.10})$$

subject to the same boundary condition given by Eqs. A.7,A.8. Separation and integration gives.

$$U_{ss} = -\frac{G}{6}\rho^3 + C_1\rho + C_2 \quad (\text{A.11})$$

Applying Eq. A.8 directly gives  $C_2 = 0$  and, with some algebra Eq. A.7 gives,

$$C_1 = \left( \frac{G}{6} + \frac{G}{3\text{Bi}} \right)$$

valid for  $\text{Bi} > 0$ . Thus the steady-state distribution of our transformed variable is

$$U_{ss} = \left( \frac{G}{6} + \frac{G}{3\text{Bi}} - \rho^2 \right) \rho \quad (\text{A.12})$$

The next step is to find the homogeneous solution of

$$\frac{\partial^2 U_h}{\partial \rho^2} = \frac{\partial U_h}{\partial \tau} \quad (\text{A.13})$$

Again, subject to Eqs. A.7,A.8, but now with a modified initial condition of

$$\begin{aligned} U_{h,0} &= U_0 - U_{ss} \\ &= \left[ 1 - \left( \frac{G}{6} + \frac{G}{3\text{Bi}} - \rho^2 \right) \right] \rho \end{aligned} \quad (\text{A.14})$$

This is a standard homogeneous partial differential equation. The solution is of the form

$$U_h = R(\rho)\Gamma(\tau) \quad (\text{A.15})$$

The solution for  $\Gamma$  is given as

$$\Gamma = \exp(-\zeta^2\tau) \quad (\text{A.16})$$

The space-variable function  $R(\zeta, \rho)$  satisfies the following eigenvalue problem:

$$\frac{d^2R}{d\rho^2} + \zeta^2 R = 0 \quad (\text{A.17})$$

subject to

$$R_{\rho=0} = 0 \quad (\text{A.18})$$

and

$$\left[ \frac{dR}{d\rho} + (\text{Bi} - 1)R \right]_{\rho=1} = 0 \quad (\text{A.19})$$

This eigenvalue problem is a special case of the Sturm-Liouville problem. The solution for  $U_h$  can be constructed from known eigenvalue solutions,

$$U_h(\rho, \tau) = \sum_{n=1}^{\infty} c_n R(\zeta_n, \rho) \exp(-\zeta_n^2 \tau) \quad (\text{A.20})$$

Application of the initial condition gives,

$$F(\rho) = \sum_{n=1}^{\infty} c_n R(\zeta_n, \rho) \quad (\text{A.21})$$

where  $F(\rho)$  is the initial condition defined from Eq A.9,

$$F(\rho) = \left[ 1 - \frac{G}{6} \left( 1 + \frac{2}{\text{Bi}} - \rho^2 \right) \right] \rho \quad (\text{A.22})$$

The coefficients of  $c_n$  can be determined by applying the operator  $\int_0^1 R(\zeta_n, \rho) d\rho$  and utilizing the orthogonality property of eigenfunctions. The coefficients are found in the form

$$c_n = \frac{1}{N(\zeta_n)} \int_0^1 R(\zeta_n, \rho') F(\rho') d\rho' \quad (\text{A.23})$$

The norm,  $N$  is a function of the eigenvalues,

$$N(\zeta_n) = \int_0^1 [R(\zeta_n, \rho)]^2 d\rho \quad (\text{A.24})$$

The eigenfunctions for Eq. A.17 are

$$R(\zeta_n, \rho) = \sin(\zeta_n \rho) \quad (\text{A.25})$$

where the eigenvalues are the root of the following transcendental equation,

$$\zeta_n \cot(\zeta_n) = -H \quad (\text{A.26})$$

the roots of which will be found numerically. The normalization integral is then solved as

$$\frac{1}{N(\zeta_n)} = 2 \frac{\zeta_n^2 + H^2}{\zeta_n^2 + H^2 + H} \quad (\text{A.27})$$

where  $H = (\text{Bi} - 1)$ .

We substitute the coefficients of Eq. A.23, they can be substituted back into Eq. A.20 and we have a solution for the homogeneous, transient distribution,

$$U_h(\rho, \tau) = \sum_{n=1}^{\infty} \exp(-\zeta_n^2 \tau) \frac{R(\zeta_n, \rho)}{N(\zeta_n)} \int_0^1 R(\zeta_n, \rho') F(\rho') d\rho' \quad (\text{A.28})$$

In order to explicitly express the solution, we will first set the integral equal to a function  $Z(\zeta_n)$  and evaluate as,

$$\begin{aligned} Z(\zeta_n) &= \int_0^1 R(\zeta_n, \rho') F(\rho') d\rho' \\ &= \int_0^1 \sin(\zeta_n \rho') \left[ 1 - \left( \frac{G}{6} + \frac{G}{3\text{Bi}} - \rho'^2 \right) \right] \rho' d\rho' \\ &= \left[ 1 - \left( \frac{G}{6} + \frac{G}{3\text{Bi}} \right) \right] \int_0^1 \sin(\zeta_n \rho') \rho' d\rho' + \frac{G}{6} \int_0^1 \sin(\zeta_n \rho') \rho'^3 d\rho' \end{aligned} \quad (\text{A.29})$$

The two unique integrals are evaluated as

$$\begin{aligned} C_n &= \int_0^1 \sin(\zeta_n \rho') \rho' d\rho' = \frac{\sin \zeta_n - \zeta_n \cos \zeta_n}{\zeta_n^2} \\ K_n &= \int_0^1 \sin(\zeta_n \rho') \rho'^3 d\rho' = \frac{3(\zeta_n^2 - 2) \sin \zeta_n - \zeta_n(\zeta_n^2 - 6) \cos \zeta_n}{\zeta_n^4} \end{aligned}$$

Thus our  $Z$  function is

$$Z(\zeta_n) = \left[ 1 - \left( \frac{G}{6} + \frac{G}{3\text{Bi}} \right) \right] C_n + \frac{G}{6} K_n \quad (\text{A.30})$$

The homogeneous solution is then written in a compact form as,

$$U_h(\rho, \tau) = \sum_{n=1}^{\infty} \exp(-\zeta_n^2 \tau) \sin(\zeta_n \rho) \frac{Z(\zeta_n)}{N(\zeta_n)} \quad (\text{A.31})$$

The complete solution is then a superposition of Eq. A.12 and Eq. A.31,

$$U(\rho, \tau) = \left( \frac{G}{6} + \frac{G}{3\text{Bi}} - \rho^2 \right) \rho + \sum_{n=1}^{\infty} \exp(-\zeta_n^2 \tau) \sin(\zeta_n \rho) \frac{Z(\zeta_n)}{N(\zeta_n)} \quad (\text{A.32})$$

We now transform back to our dimensionless temperature,

$$\theta(\rho, \tau) = \left( \frac{G}{6} + \frac{G}{3\text{Bi}} - \rho^2 \right) + \sum_{n=1}^{\infty} \exp(-\zeta_n^2 \tau) \frac{\sin(\zeta_n \rho)}{\rho} \frac{Z(\zeta_n)}{N(\zeta_n)} \quad (\text{A.33})$$

### A.3 Energy

We will want to compare the solution of Eq. A.33 to that of a sphere with the lumped capacitance assumption. To facilitate comparison, we look to a measure of the energy of the sphere (with radial dependence removed via integration of Eq. A.33). The energy will be nondimensionalized as,

$$E^*(\tau) = \frac{E(\tau)}{E_0} \quad (\text{A.34})$$

where  $E_0$  is the initial energy of the sphere,

$$E_0 = \rho_r C_r V \mathbb{T}_0 \quad (\text{A.35})$$

Thus the nondimensional energy of the sphere at a given time,  $\tau$  is

$$\begin{aligned} E^*(\tau) &= \int \frac{\rho_r C_r \mathbb{T}(\rho, \tau) dV}{\rho_r C_r V \mathbb{T}_0} \\ E^*(\tau) &= \frac{1}{V} \int \theta(\rho, \tau) dV \end{aligned} \quad (\text{A.36})$$

For a circle in spherical coordinates:

$$dV = r^2 \sin(\phi) dr d\phi d\theta \quad (\text{A.37})$$

For our sphere, this becomes:

$$dV = 4\pi b^3 \rho^2 d\rho = 3V \rho^2 d\rho \quad (\text{A.38})$$

The integral for dimensionless energy of our sphere is then,

$$E = 3 \int_0^1 \left[ \frac{G}{6} \left( 1 + \frac{2}{\text{Bi}} - \rho^2 \right) + \sum_{n=1}^{\infty} \exp(-\zeta_n^2 \tau) \frac{\sin(\zeta_n \rho)}{\rho} \frac{Z(\zeta_n)}{N(\zeta_n)} \right] \rho^2 d\rho \quad (\text{A.39})$$

This ultimately reduces to,

$$E^* = \left( \frac{G}{15} + \frac{G}{3\text{Bi}} \right) + 3 \sum_{n=1}^{\infty} \exp(-\zeta_n^2 \tau) \frac{Z(\zeta_n)}{N(\zeta_n)} C_n(\zeta_n) \quad (\text{A.40})$$